

Microphysical properties and light absorption enhancement of refractory black carbon aerosols in the central Arctic marine boundary layer: role of warm airmass intrusions on mixing state

Babu Suja Arun¹, Thomas Müller¹, Mira L. Pöhlker^{1,2}, Andreas Held³, Christopher Pöhlker⁴, Manuela van Pinxteren¹, Yifan Yang¹, Sabine Lühtrath³, Andreas Walbröl⁵, Janna E. Rückert⁶, Philipp Oehlke¹, Maik Merkel¹, and Birgit Wehner¹

¹Leibniz Institute for Tropospheric Research, Leipzig, Germany

²Faculty of Physics and Earth Sciences, Leipzig Institute for Meteorology, Leipzig University, Leipzig, Germany

³Environmental Chemistry and Air Research, Technische Universität Berlin, Berlin, Germany

⁴Max Planck institute for Chemistry, Mainz, Germany

⁵Institute for Geophysics and Meteorology, University of Cologne, Cologne, Germany

⁶Institute of Environmental Physics, University of Bremen, Bremen, Germany

Correspondence: Babu Suja Arun (arun.babu@tropos.de)

Received: 31 December 2025 – Discussion started: 21 January 2026

Revised: 16 April 2026 – Accepted: 25 April 2026 – Published:

Abstract. **TSI** Refractory black carbon (rBC) aerosol particles strongly influence Arctic atmospheric radiative transfer, making it essential to understand their microphysical properties and mixing state. However, in-situ investigations on microphysical properties and mixing state of rBC particles over the central Arctic marine boundary layer are scarce. To address this gap, we carried out a comprehensive investigation of rBC particles in the central Arctic onboard the RV *Polarstern* during the ATWAICE cruise. Our results revealed pronounced spatial and temporal variability in microphysical properties rBC in the Arctic marine boundary layer, governed by transport pathways and removal mechanisms. Under pristine background conditions, rBC mass concentrations were at their lowest (median $\sim 0.4\text{--}0.6\text{ ng m}^{-3}$). The mass median diameter of rBC cores was found to increase with latitude, from the lowest value ($\sim 156\text{ nm}$) in lower-latitude regions influenced by higher anthropogenic emissions to $\sim 220\text{ nm}$ in the high Arctic, consistent with the persistence of aged aerosols under background conditions. Warm airmass intrusions into the Arctic atmosphere were found to bring polluted anthropogenic aerosols into this pristine environment with an eightfold increase in rBC mass concentrations (median $\sim 3.4\text{ ng m}^{-3}$, $\text{rBC}_{\text{max}} \sim 74\text{ ng m}^{-3}$). A dominant influence of biomass-burning emissions from Eurasia during the warm airmass intrusion, which coincided with a shift toward larger rBC cores ($\sim 264\text{ nm}$) and moderate coating thickness. The light absorption enhancement of rBC estimated using core-shell Mie theory remained low during warm airmass intrusions ($\sim 1\text{--}1.2$) than under background conditions ($\sim 1.1\text{--}1.6$), underscoring a strong dependence of rBC radiative effects in the central Arctic on source regions and aging/processing during long-range transport. This study highlights the complexity of rBC aging and mixing state in the central Arctic, driven by variable source characteristics and summertime processing conditions and will help to increase the accuracy in representing rBC in climate models.

1 Introduction

The Arctic region is experiencing accelerated warming, a phenomenon known as Arctic Amplification. Over the past four decades, this has led to a nearly fourfold increase in surface air temperatures over the Arctic (Rantanen et al., 2022). Many climatic feedback mechanisms contribute to this process, involving interactions between the atmosphere, cryosphere, biosphere, and ocean. The key contributors to Arctic amplification include the decline in sea ice extent and thickness, changes in surface albedo, meridional atmospheric moisture transport, ocean heat transport, and alterations in cloud characteristics (Woods and Caballero, 2016; Beer et al., 2020; Zhang et al., 2018a; Thackeray and Hall, 2019; Wendisch et al., 2023). Although greenhouse gases are the primary driver of global warming, atmospheric aerosol particles significantly impact the Arctic climate by influencing the radiative balance through the scattering and absorption of solar radiation, cloud formation, and deposition processes (Haywood and Boucher, 2000; Schmale et al., 2021). The radiative impact of aerosols varies seasonally in the Arctic, as cloud cover, surface reflectivity, and solar radiation fluctuate throughout the year (Quinn et al., 2008; Flanner, 2013). The Arctic aerosol life cycle is highly seasonal, primarily driven by long-range transport, atmospheric processing, and precipitation scavenging (Tunved et al., 2013). Elevated aerosol loadings were found during the Arctic haze period, when aerosol particles were primarily transported from industrialized regions of Eurasia and North America under stable atmospheric conditions (Stohl, 2006). During summer, Arctic aerosols undergo extensive wet scavenging, while photochemical activity and biogenic emissions stimulate new particle formation (Engvall et al., 2008). Low-level clouds contribute to winter and early spring warming by trapping outgoing longwave radiation; whereas in summer, they exert a cooling effect by reflecting incoming solar energy (Zhao and Garrett, 2015). Light-absorbing aerosols can amplify these effects, raising atmospheric temperatures and potentially dissipating clouds (Sand et al., 2013).

One of the most significant climate-forcing aerosol components in the Arctic is black carbon (BC), which is produced by the incomplete combustion of fossil fuels and biomass (Bond et al., 2013). BC contributes to atmospheric warming mainly through three mechanisms: absorbing solar radiation (direct effect), altering cloud properties (indirect effect), and reducing snow and ice albedo when deposited on these highly reflective surfaces (albedo effect) (Flanner, 2013; Sand et al., 2013; Thakur et al., 2021; Gustafsson et al., 2026). Due to the limited number of local BC sources in the Arctic, the majority of BC is transported from mid-latitude regions (Bozem et al., 2019; Croft et al., 2016; Gogoi et al., 2021; Pernov et al., 2022). BC transport into the Arctic lower troposphere is influenced by synoptic-scale circulation patterns and boundary-layer dynamics, with wet scavenging as the

dominant removal mechanism (Garrett et al., 2011; Winiger et al., 2017).

The atmospheric lifetime, radiative impact, and cloud-interaction potential of BC aerosols are critically influenced by their microphysical properties, particularly size and mixing state (Ching et al., 2016; Asmi et al., 2025). Freshly emitted BC is typically hydrophobic and externally mixed. In contrast, during atmospheric transport, it undergoes aging via condensation and coagulation, acquiring coatings of organic and inorganic species that enhance its hygroscopicity and cloud condensation nuclei activity (Nenes et al., 2002; Motos et al., 2019a). This transformation not only alters the light absorption efficiency of BC but also modulates its susceptibility to wet scavenging processes, especially nucleation scavenging within clouds (Matsui, 2016; Motos et al., 2019b). BC aging timescales are governed by atmospheric oxidant levels and precursor vapours, both of which vary seasonally and regionally (Fierce et al., 2015). In the Arctic summer, despite higher photochemical activity, enhanced low-level cloudiness and fog formation may accelerate wet removal of aged BC, allowing relatively fresh or partially aged particles to dominate. Yet, the extent and rate at which BC becomes internally mixed in the Arctic marine boundary layer remain poorly understood. Understanding these microphysical transformations is essential to reduce uncertainties in Arctic BC radiative forcing, especially as climate models often simplify or misrepresent BC aging and removal processes (Ching et al., 2018).

Recent assessments have highlighted substantial uncertainties in Arctic BC emissions, primarily due to the underrepresentation of key sources such as gas flaring, waste burning, and mobile combustion in emission inventories (Schmale et al., 2018). For example, flaring emissions from northern Russia may contribute up to 66% of Arctic BC; however, isotope analyses suggest that this estimate may be too high due to errors in emission factors and spatial distribution (Winiger et al., 2017). Emission inventories vary by up to a factor of three (AMAP, 2015; Schmale et al., 2018), further compounding modelling uncertainties. In addition to emission uncertainties, the transformation of BC through atmospheric aging remains poorly constrained in Arctic conditions. This is particularly relevant in the Arctic MBL, where low temperatures and limited precursor gas concentrations slow BC aging (Fierce et al., 2016), and where summer fog and low-level cloudiness can enhance wet scavenging. Consequently, understanding how BC evolves microphysically, especially how it becomes internally mixed and activates as cloud condensation nuclei, remains a major knowledge gap. These microphysical changes critically influence the radiative efficiency of BC, its atmospheric lifetime, and its eventual deposition.

Despite advances in understanding Arctic aerosols, significant uncertainties remain in understanding BC aerosols and their climatic impacts, particularly regarding their interactions with clouds, transport pathways, and deposition

processes, due to limited knowledge of the microphysical properties of BC. There exist long-term ground-based BC measurements from a network of Arctic observatories (e.g., Zeppelin, Ny-Ålesund, Pallas, Barrow, Alert, Tiksi, etc.) (Sharma et al., 2006; Eleftheriadis et al., 2009; Schmeisser et al., 2018; Gogoi et al., 2021), and in recent years numerous aerosol observations have also been made over the Arctic using ground-based stations, aircraft campaigns and ship-borne platforms (Raatikainen et al., 2015; Schulz et al., 2019; Park et al., 2020; Jurányi et al., 2022, 2023; Zanatta et al., 2023; Heutte et al., 2023; Zieger et al., 2023). However, even now, the detailed understanding of the microphysical properties of refractory BC (rBC) particles remains scarce, especially in the central Arctic marine boundary layer (MBL). With this in mind, we have conducted the aerosol observations onboard RV *Polarstern* (PS131) in the central Arctic during summer 2022 to understand the microphysical properties and mixing state of rBC particles in the central Arctic MBL. This study investigates the rBC loading, its size distribution, mixing state, and light-absorption enhancement in the central Arctic MBL, with a particular focus on the role of warm air mass intrusions in modulating the microphysical properties of rBC.

2 Experimental details

2.1 Study region and general meteorological conditions

Ambient atmospheric aerosol measurements were conducted over the Arctic Ocean aboard the icebreaker RV *Polarstern* (PS131), operated by Alfred Wegener Institute, Germany. The expedition PS131 named ATLantic Water pathways to the ICE in the Nansen basin and Fram Strait (ATWAICE) to the central Arctic, was carried out during the summer period (28 June to 17 August 2022), during which aerosol measurements were conducted from 29 June to 12 August. The ship track during the campaign is shown in Fig. 1. The cruise covered the Arctic Ocean (including both the North Sea and the Greenland Sea) and the remote north-western Greenland Sea. *Polarstern* crossed the Arctic Circle during the night of 2 July and proceeded towards the eastern Fram Strait, where it navigated between 5 and 10 July through the warm, saline waters of the west Spitsbergen current. By 11 July, *Polarstern* reached the continental slope north of Svalbard, continuing northwest into denser ice on 12 July. On 22 July, *Polarstern* travelled northwest to the Gakkel ridge, reaching the expedition's northernmost point on 25 July. The southward transit towards the Fram Strait began on 2 August. More details about ATWAICE cruise and research area are provided in Kanzow (2023).

Figure S1 in the Supplement illustrates the temporal evolution of meteorological parameters measured aboard RV *Polarstern* during the expedition. Wind speeds generally ranged between 4 and 14 m s⁻¹ during the observation period, with several transient peaks exceeding 12 m s⁻¹, notably around

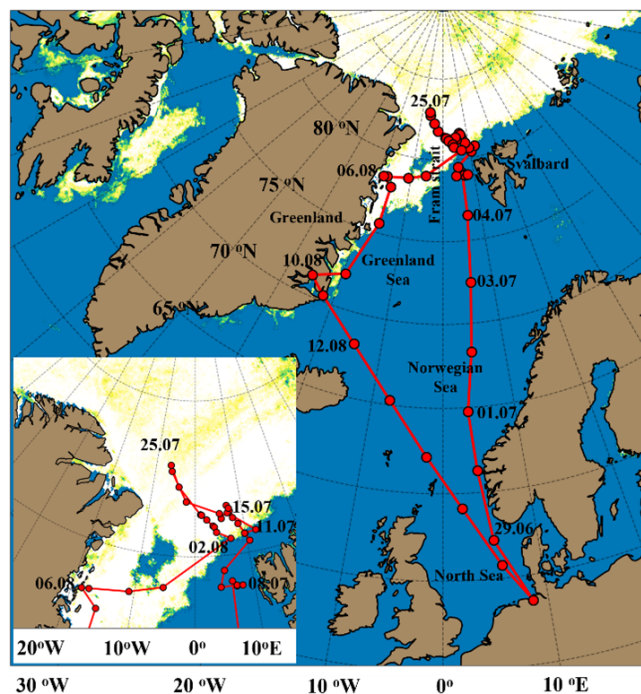


Figure 1. Ship track of RV *Polarstern* during the ATWAICE cruise from 28 June to 17 August 2022. The red line indicates the cruise trajectory, with red circle symbols marking the ship's position at local noon each day. The inset shows a zoomed-in view of the northernmost cruise tracks. Background colour indicates Sea ice concentration (MODIS-AMSR2; Ludwig et al., 2020).

7 to 9 July, 16 to 18 July, and 6 to 8 August. At the beginning of the cruise, while the ship was in the sub-Arctic latitudes and the Norwegian Sea, air temperatures were relatively high (~ 10 to 18 °C), accompanied by moderate relative humidity (RH) values ($\sim 60\%$ – 80%). As the vessel advanced northward into the marginal ice zone and eventually the central Arctic, a marked and sustained drop in temperature occurred beginning around 3 to 5 July, stabilizing around or below 2 – 5 °C throughout much of mid-to-late July. During this same period, RH increased significantly, frequently exceeding 90% , indicating a colder, more saturated boundary layer consistent with ice-covered or near-ice environments. A notably colder and humid period is observed from approximately 23 to 30 July, coinciding with the ship's passage through densely packed sea ice. Mid July (around 15 to 20 July) shows an interesting deviation from the preceding trend, marked by temperature increase (up to ~ 8 °C) and more variable RH, associated with a warm air mass intrusion over the marginal ice zone. Toward the end of the cruise in early August, another warming phase is noted, particularly from 30 July to 3 August, when the ship transitioned from ice-covered regions to open-ocean conditions. More details regarding the ATWAICE cruise are available elsewhere (Kanzow, 2023).

2.2 Measurements of aerosol particles

The measurements of aerosol particles were made from the specifically configured aerosol measurement container on the “Peildeck” of the ship, with the instruments sampling the air from a common aerosol inlet. To minimize the influence of ambient moisture, Nafion membrane dryers were integrated into the sampling system, maintaining the relative humidity of the sampled air below 40%. Measurements of rBC particles were performed using a Single Particle Soot Photometer (SP2, Model: SP2-D; Droplet Measurement Technologies, USA), which operates at 0.12 L min^{-1} . SP2 utilizes the laser-induced incandescence technique to measure rBC properties using an Nd:YAG laser at 1064 nm (Schwarz et al., 2008). The amplitude of the incandescence signal from SP2 is proportional to the rBC mass present in BC-containing particles (Schwarz et al., 2008).

The leading-edge-only (LEO) fitting technique is commonly employed to reconstruct the scattering signal from SP2 (Gao et al., 2007; Liu et al., 2014) to understand the mixing state of rBC. The reconstructed signal is compared with Mie model values to derive the size of coated BC particles. In this approach, the particle is assumed to exhibit a concentric core-shell morphology, represented as a sphere with the core having a refractive index of $2.26-1.26i$ and the coating set at $1.5 + 0i$ (Moteki et al., 2010). The BC core diameter (D_c) is estimated based on an assumed atmospheric BC density of 1.8 g cm^{-3} (Moteki and Kondo, 2010), while the amplitude of the scattering signal provides information about the scattering cross section of the particles, which is used to derive the optical sizing of the particles (Yang et al., 2025). Prior to measurements, the SP2 was calibrated using Aquadag® black carbon standards, with a correction factor of 0.75 applied to account for differences from ambient BC (Baumgardner et al., 2012; Laborde et al., 2012; Yang et al., 2025). The coating thickness of BC-containing particles is inferred by comparing the optical diameter (D_p) and the D_c .

The absolute coating thickness (CT) is estimated as,

$$\text{CT} = (D_p - D_c)/2 \quad (1)$$

The mass median diameter (MMD) is determined by fitting BC core size distributions to a monomodal log-normal distribution function (Liu et al., 2019).

To understand the size-resolved coating thickness of rBC particles during the study period, the rBC particles were classified into an $i \times j$ grid with i bins for rBC core diameter and j bins for coating thickness. The total volume of rBC containing particles at each grid point is estimated as (Yang et al., 2025),

$$\begin{aligned} \text{Volume}_{\text{grid}(i,j)} &= \frac{\pi}{6} D_{p(i,j)}^3 N_{i,j} \\ &= \frac{\pi}{6} (D_{c,i} + 2 \times \text{CT}_j)^3 N_{i,j} \end{aligned} \quad (2)$$

where D_p represents the diameter of the rBC containing particle and N indicates the total number of rBC particles.

In this study, the rBC mass concentration was corrected for the missing fraction of rBC ($6 \pm 4\%$) due to the detection limit of SP2. More detailed information regarding SP2, data interpretation procedures, uncertainties, and caveats is available elsewhere (Moteki and Kondo, 2010; Yang et al., 2025).

To quantify the impacts of rBC particles in the Arctic, we calculated the absorption enhancement factor (E_{abs}) and mass absorption cross-section (MAC) of rBC particles using Mie theory, constrained by in situ single-particle measurements obtained with SP2 (Yang, 2024). The individual coating thickness was derived assuming a concentric core-shell geometry. To estimate absorption properties, we assumed that each rBC particle can be modelled as a homogeneous spherical core with a concentric, non-absorbing coating (e.g., sulfate or organics). The complex refractive index for the rBC core was set to $1.95 + 0.96i$, consistent with literature values for soot, while the coating refractive index was taken as $1.53 + 0i$ (Moteki et al., 2023; Schnaiter et al., 2005; Zhang et al., 2018b). We used a Mie scattering code based on the core-shell solution of Bohren and Huffman (1998) to compute the absorption cross-section of each size bin, both for coated ($C_{\text{abs,coated}}$) and bare ($C_{\text{abs,bare}}$) rBC particles.

The absorption enhancement factor was then calculated as:

$$E_{\text{abs}} = \frac{C_{\text{abs,coated}}}{C_{\text{abs,core}}} \quad (3)$$

This reflects the increase in light absorption caused by the lensing effect of the non-absorbing coating.

In parallel, the mass absorption cross-section (MAC) was derived using,

$$\text{MAC} = \frac{C_{\text{abs}}}{M_{\text{rBC}}}, \quad (4)$$

where M_{rBC} is the mass of the rBC core in each size bin. The MAC values were computed for both bare and coated particles, providing insight into how mixing modifies the specific absorption capacity of rBC under different atmospheric conditions. This enabled direct comparison across regimes with differing aerosol source histories, atmospheric aging states, and mixing conditions.

The light absorption enhancement (E_{abs}) estimated here is using an idealized spherical, concentric core-shell representation (Mie theory based). It should be noted that the real atmospheric BC commonly exhibits complex/fractal morphology and heterogeneous mixing/coating structures, for which core-shell Mie representations can overestimate E_{abs} values that differ from morphology resolved calculations and observations (e.g., Adachi et al., 2010; Ueda et al., 2016; Fierce et al., 2020; Wang et al., 2021; Zhang et al., 2026).

The measurements of equivalent black carbon (eBC) were performed using a multi-angle absorption photometer (MAAP), which measures transmitted and backscattered light from a particle-loaded filter (Petzold and Schönlinner,

2004). Although the MAAP directly measures the absorption coefficient, the results were converted to eBC mass concentration using a predefined mass absorption cross section. In general, eBC measurements were reported at a wavelength of 637 nm, following the recommendations of Müller et al. (2011). A correction factor of 1.05 was applied to account for systematic biases in the retrieval of eBC concentrations. Measurements of light-scattering coefficients were performed using an integrated Nephelometer (Aurora Ecotech 4000). More details regarding this instrument are available elsewhere (Müller et al., 2011).

The aerosol light scattering coefficient was measured using an integrating Nephelometer (Ecotech Aurora 4000). It measures the aerosol total scattering (σ_{sca} , between 10 and 170°) and back-scattering coefficients (between 90 and 170°) at three wavelengths (450, 525, and 635 nm). The nephelometer data was corrected following the methodology described by Müller et al. (2011). The detailed description of the main characteristics and the working principle of the integrating nephelometers can be found in Müller et al. (2011).

In addition, aerosol particle sampling was conducted using a high-volume digital aerosol sampler mounted on the rooftop of the aerosol measurement container. After sampling, the samples were stored in aluminium boxes at -20°C and transported to TROPOS, Leipzig, for further chemical analysis. To account for potential contamination during handling and transport, field blanks were prepared by loading the sampler at the sampling site without drawing air through the system. Measurements of organic carbon and elemental carbon were made using a Sunset OC-EC analyser following the EUSAAR II TOT protocol (Birch and Cary, 1996). The concentrations of selected inorganic species were determined in filtered aqueous extracts (0.45 μm syringe filters, 50 % of the filter extracted in 2 mL ultrapure water) using ion chromatography (ICS3000, Dionex, Sunnyvale, CA, USA), following the methodology described by Müller et al. (2010). Regular instrument calibration and quality control procedures were implemented to ensure the accuracy and reliability of the analytical measurements.

Ship plumes were occasionally detected during the campaign. To ensure that aerosol measurements were not influenced by emissions from the ship's exhaust, the sampling inlet was installed ahead of the ship's engines. Despite this strategic placement, some data points were still affected by ship emissions and had to be filtered out before further analysis to obtain a dataset representing background aerosol concentrations. The following conditions led to data exclusion: Data points were removed when the relative wind direction ranged between 110 and 260°, as this wind pattern could carry exhaust emissions toward the sampling inlet. Measurements taken at wind speeds below 2 m s^{-1} were discarded since weak winds can cause local turbulence, increasing the risk of exhaust contamination. Sharp increases or abrupt fluctuations in total particle number concentration were considered indicative of contamination and were there-

fore excluded. Any extreme spikes in the incandescence signal from SP2 were removed, as they were likely linked to ship exhaust plumes. For offline aerosol sampling, an automated pollution-avoidance system was used. This system, which continuously monitored relative wind direction, was integrated with the digital sampler to automatically halt the sampling pumps when airflow originated from the sector associated with ship exhaust contamination.

2.3 Thermodynamic measurements of the atmosphere

A Humidity and Temperature PROfiler (HATPRO) microwave radiometer (Rose et al., 2005) was deployed on the Peildeck, adjacent to the aerosol measurement container during the cruise. This instrument continuously measures atmospheric radiances emitted by water vapor, oxygen, and liquid cloud droplets, utilizing seven frequencies between 22 and 31 GHz along a water vapor absorption line and seven additional channels between 51 and 58 GHz within the oxygen absorption complex. With a high temporal resolution of approximately 1 s, HATPRO provides near-continuous monitoring of key atmospheric variables. The primary observational mode involved zenith-pointing measurements, enabling the retrieval of vertically integrated water vapor (IWV), liquid water path (LWP), and vertical profiles of temperature and absolute humidity following established methodologies (e.g., Walbröl et al., 2022). In a shorter observational mode for 15 consecutive minutes each hour, the instrument was observing the surface, and no measurements of the atmosphere were recorded. Additionally, boundary layer scanning at multiple elevation angles was conducted to enhance temperature profiling within the lower troposphere.

3 Results and discussion

3.1 Latitudinal variability and source signatures of aerosol particles

Figure 2 shows the temporal evolution of the aerosol light scattering coefficient at 525 nm (σ_{sca}), mass concentrations of equivalent black carbon (eBC) and refractory black carbon (rBC) along the cruise track. σ_{sca} , eBC and rBC exhibited pronounced variability during the campaign, with comparatively high values during the initial, lower-latitude part of the transect and substantially lower values over the central Arctic.

The hourly σ_{sca} ranged from 0.1 and 66 Mm^{-1} , with approximately 90 % of the observations below 25 Mm^{-1} . Higher σ_{sca} values observed during the beginning of the campaign, whereas σ_{sca} remained mostly below 10 Mm^{-1} over much of the high Arctic. As the research vessel moved to northern latitudes, σ_{sca} generally decreased and remained low over large parts of the central Arctic. This behaviour is consistent with previous summertime observations in the Arctic reporting low aerosol loadings in the central Arctic

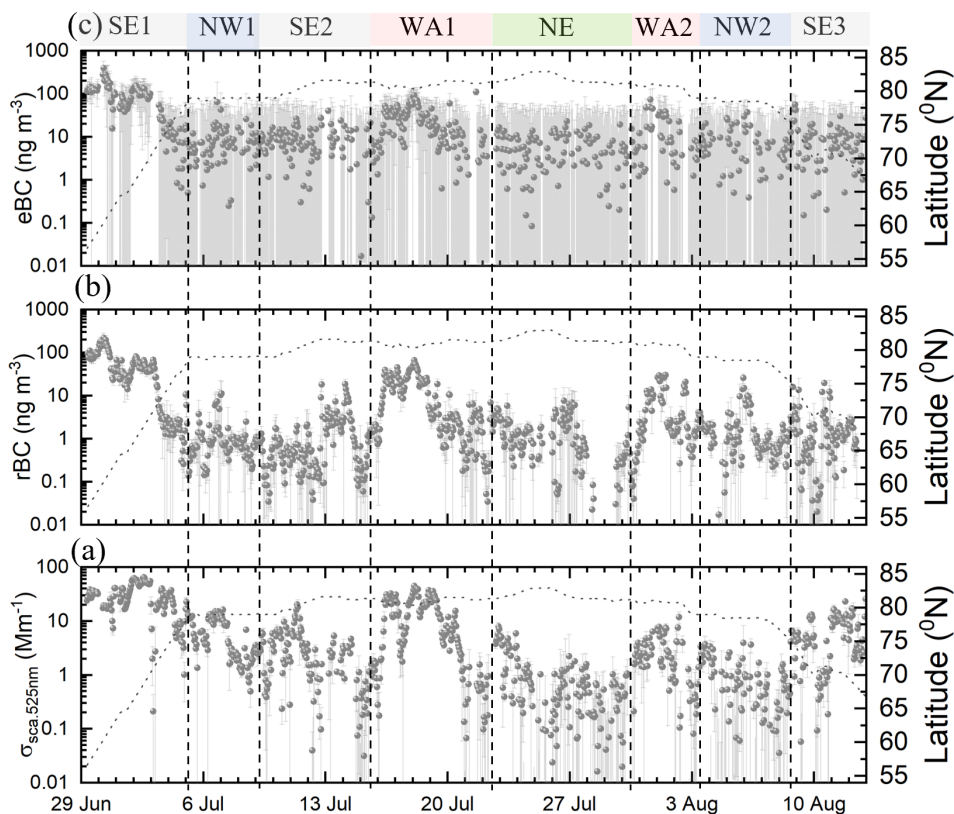


Figure 2. (a) Light scattering coefficient of aerosols measured at wavelength 525 nm using an integrating Nephelometer, (b) Refractory black carbon mass concentration measured using SP2, (c) Equivalent black carbon mass concentration measured using MAAP. Each subplot is accompanied by a dotted line indicating the corresponding latitude (right y-axis). The vertical grey lines indicate the respective standard deviation for each parameter.

compared with lower-latitude regions influenced by marine and continental airmasses (Quinn et al., 2002; Tomasi et al., 2007; Schmeisser et al., 2018; Pandolfi et al., 2018; Gogoi et al., 2021; Schmale et al., 2022).

5 The temporal variability of eBC and rBC broadly followed that of σ_{sca} . During the initial phase of the cruise (29 June–3 July), when the ship was located at lower latitudes, eBC frequently exceeded 100 ng m^{-3} , with a maximum of 399 ng m^{-3} . North of approximately 70° N , eBC
 10 decreased significantly, and 95 % of the subsequent observations remained below 40 ng m^{-3} . The rBC mass concentration (MrBC) exhibited a similar large-scale pattern, with enhanced values during the lower-latitude part of the transect and low concentrations during the observations in the central Arctic. Nonetheless, episodes of enhanced σ_{sca} , eBC, and
 15 rBC were observed from 15 to 22 July and 30 July to 3 August, suggesting the transient influence of warm airmass intrusions favourable for enhanced aerosol loadings. This will be discussed in detail in Sect. 3.2.

20 Although eBC and rBC covaried during the campaign, differences were evident in their absolute magnitudes and short-term variability. These differences likely reflect the distinct measurement principles of the MAAP and SP2, as well as

differences in their sensitivity to particle mixing state and aerosol composition (Backman et al., 2017; Asmi et al., 2021, 2025). The correlation between eBC and rBC measured during the study period are provided in the supplementary information (Fig. S2). In addition, elemental carbon (EC) derived from filter samples was mostly below the detection limit of the OC-EC analyser throughout the campaign
 25 (Fig. S3), indicating that filter-based EC measurements had limited applicability under the very low aerosol loadings encountered here. For this reason, the following discussion focuses primarily on SP2-derived rBC, which provides higher sensitivity and time resolution under background Arctic conditions.
 30
 35

In order to understand the observed variability in the context of airmass transport pathways, 5 d backward airmass trajectories arriving at the ship position ($\sim 100 \text{ m a.s.l.}$) were calculated using NOAA Hybrid Single-Particle Lagrangian Integrated Trajectory model (HYSPPLIT) (Stein et al., 2015) overlaid on the Arctic Sea ice concentration data from MODIS-AMSR2 (Spreen et al., 2008; Ludwig et al., 2020) during the cruise period. This is further grouped into eight consecutive airmass transport regimes (SE1 – South
 40
 45 easterly 1, NW1 – North westerly 1, SE2 – South easterly

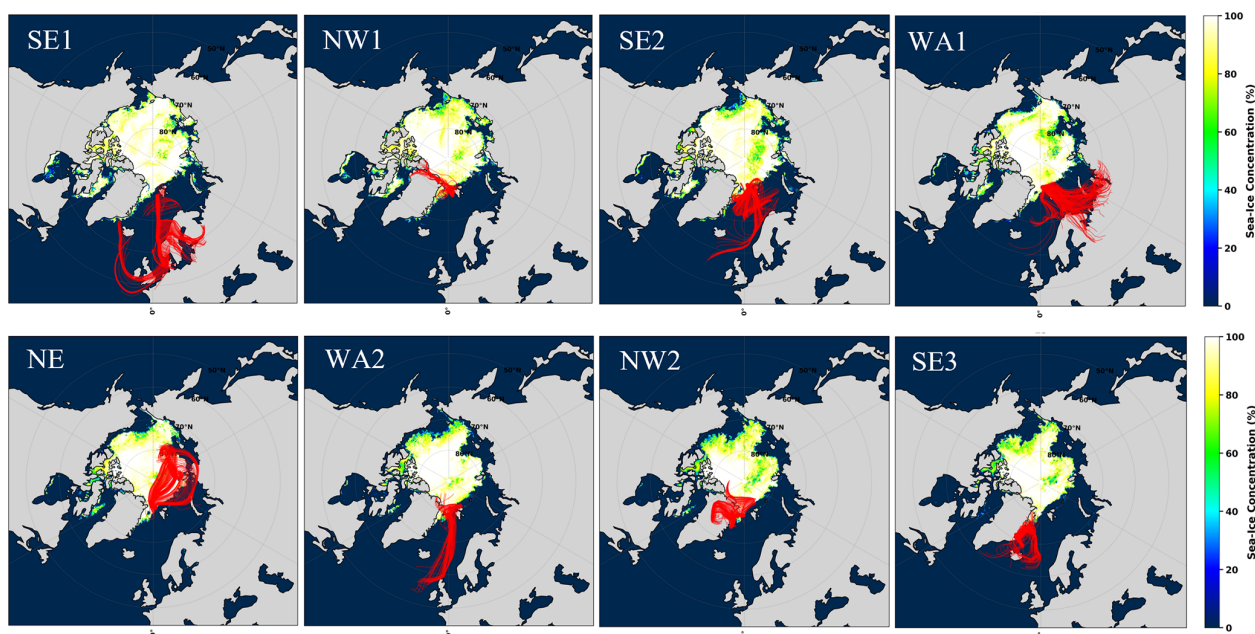


Figure 3. 5 d backward air mass trajectories arriving at the ship position during the campaign segregated into different continuous air mass regimes (SE1 – South easterly 1, NW1 – North westerly 1, SE2 – South easterly 2, WA1 – Warm airmass intrusion 1, NE – North easterly, WA2 – Warm airmass intrusion 2, NW2 – North westerly 2, SE3 – South easterly 3) during the study period.

2, WA1 – Warm airmass intrusion 1, NE – North easterly, WA2 Warm airmass intrusion 2, NW2 – North westerly 2, and SE3 – South easterly 3; Fig. 3). These regimes differ in their dominant transport direction and in the relative time spent over continental, marine, and sea-ice covered surfaces. Figure 4a summarizes the fractional contribution of relative time each air mass regimes spent over these three different surface types.

Among all regimes, SE1 showed the highest rBC concentrations (median $\sim 37 \text{ ng m}^{-3}$; Fig. 4b). Air masses during this period indicate transport from lower-latitude regions with a stronger continental influence than during the central Arctic regimes, together with substantial residence time over marine environments. This regime was also characterized by elevated σ_{sca} ($\sim 36 \text{ Mm}^{-1}$) and a comparatively large contribution of Na^+ and Cl^- to the bulk aerosol composition (Fig. 5), suggesting the simultaneous presence of combustion related aerosols and sea-salt-containing particles. Interpretation of σ_{sca} variability based solely on PM_{10} bulk chemical composition is inherently qualitative because aerosol light scattering depends strongly on particle size distribution and number concentration, not only on mass fraction. In particular, coarse-mode constituents (e.g., Na^+ and Cl^-) may dominate mass during marine influence, whereas fine-mode sulfate and organic aerosol can contribute significantly to σ_{sca} . Since, our chemical composition of PM_{10} samples represents bulk, 24 h integrated composition across a broad size range, the discussion of it with respect to σ_{sca} is qualitative; scattering depends strongly on particle size distribution and number

concentration, and we therefore do not attempt size or component resolved attribution with this. The higher rBC loading observed during SE1 likely reflects the influence of continental outflow and possible shipping emissions, as the measurements were at lower latitudes closer to coastal regions.

In contrast, SE2 and NE were characterized by the lowest rBC concentrations. SE2 was dominated by air mass transport over marine regions (88 %) with limited continental influence ($\sim 5 \%$), whereas NE was associated with air masses travelling largely within the central Arctic, including over sea-ice-covered regions ($\sim 64 \%$ marine and $\sim 33 \%$ sea ice). During both regimes, rBC concentrations remained very low, typically below $\sim 0.6 \text{ ng m}^{-3}$, and σ_{sca} was also low ($\sim 1 \text{ Mm}^{-1}$), particularly during NE. These observations indicate a weak influence of combustion sources with the generally clean summertime central Arctic boundary layer. The lower σ_{sca} ($\sim 1 \text{ Mm}^{-1}$) during NE may additionally reflect a reduced contribution from open-ocean derived aerosol since it traversed significantly through sea ice covered regions.

The NW1, NW2, and SE3 regimes showed intermediate behaviour in rBC properties in comparison with other regimes. The rBC concentrations during these periods were higher than those observed during SE2 and NE, but substantially lower than those during SE1. The air mass transport during this period indicates mixed transport pathways involving different combinations of marine, sea-ice, and more limited continental influence. The low to modest rBC concentrations observed in these regimes suggest either limited source influence, efficient scavenging during transport, or a

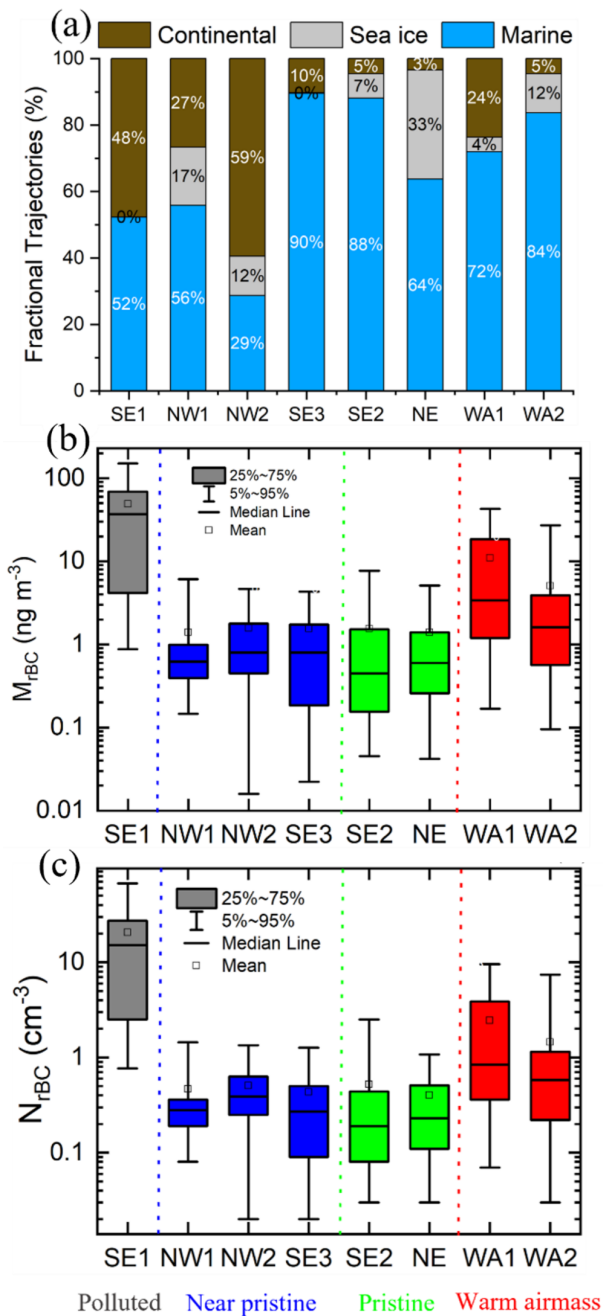


Figure 4. (a) Stacked bar plots representing the fractional contributions of three different surface types traversed by airmasses before arriving at each of the eight designated airmass regimes: SE1, NW1, NW2, SE3, SE2, NE, WA1 and WA2. The three categories are: Marine (Blue): Airmasses that predominantly travelled over oceanic regions. Sea Ice (Gray): Airmasses that passed over areas covered by sea ice. Continental (Brown): Airmasses influenced by land surfaces. Each bar is segmented and annotated with percentage values indicating the proportion of time the airmasses spent over each surface type before reaching the measurement location, (b) Box and whisker diagram showing the variabilities in mass concentration of refractory BC, (c) Box and whisker diagram showing the variabilities in number concentration of rBC particles in each regime.

combination of both. For example, although NW2 exhibited a relatively strong continental influence, the corresponding rBC concentration remained low. This indicates that longer residence time over continental surfaces did not necessarily translate into enhanced rBC concentrations at the receptor site. It is also important to note that the airmasses during this period passed over comparatively remote regions of Greenland, which may have contributed to the observed lower rBC loading. The warm airmass intrusion periods (WA1 and WA2) were associated with episodic enhancements in aerosol properties relative to the surrounding central Arctic background. These events involving additional synoptic-scale influences are discussed separately in the subsequent section.

Based on the airmass transport pathways with special emphasis on the relatively dominant residence time over the continental and sea ice surface type, in addition to the rBC concentrations, we have segregated the distinct regimes as, polluted (SE1), near-pristine (NW1, NW2 and SE3), pristine (SE2 and NE) and warm airmass intrusions (WA1 and WA2). The aerosol measurements 29 June to 5 July is marked as “polluted” whereas the observations NW1, NW2 and SE3 during 5 to 9 July, 3 to 12 August is marked as “near-pristine” and observations during 9 to 15 July and 22 to 30 July is marked as “pristine”. The measurements during warm airmass intrusion period of 15 to 22 July and 30 July to 3 August is marked as WA1 and WA2.

3.2 Warm airmass intrusions and refractory BC

Two warm airmass intrusion periods were observed during the study period, and both were associated with clear changes in thermodynamic conditions and aerosol properties over the central Arctic. These events interrupted the otherwise lower aerosol conditions that prevailed during much of the campaign and were accompanied by enhanced temperature and rBC concentrations. Previous studies have shown that such synoptic-scale intrusions can efficiently transport heat, moisture, and aerosol from lower latitudes into the Arctic (Mortin et al., 2016; Graham et al., 2017; Henderson et al., 2021; Dekoutsidis et al., 2024).

The vertical profiles of temperature and absolute humidity retrieved from HATPRO are shown in Fig. 6. Between 13 and 14 July, an occluded warm front associated with a low-pressure system over the North Atlantic transported warm and moist air. During this period, the temperatures reached up to about 7 °C at an altitude of ~600 m. Subsequently, during the WA1 period, two pronounced episodes of warm and humid air were observed between 15 and 17 July and between 17 and 19 July. These events were associated with consecutive low-pressure systems south of Svalbard and with strong south-easterly flow transporting warm, moist air towards Svalbard and the adjacent Arctic Ocean (Kanzow, 2023). During the second episode, temperatures reached a maximum of 18 °C at ~650 m altitude on 18 July, while in-

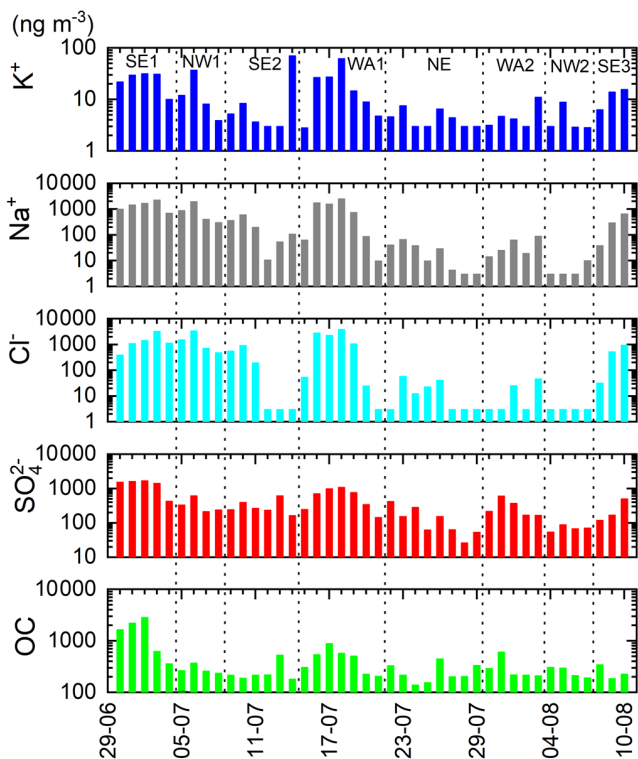


Figure 5. Mass concentration of major chemical species such as OC, SO_4^{2-} , Cl^- , Na^+ and K^+ measured during the study period.

egrated water vapour increased to 35 kg m^{-2} . During these events, *Polarstern* was mostly in open water on the lee side of Svalbard. A weaker warm air advection event followed on 19 July, but without a similarly strong increase in humidity. During WA2 (30 July to 3 August), as *Polarstern* began its transit toward the east coast of Greenland into a warm front, warm air masses were observed, with temperatures reaching up to 8°C at 850 m altitude and integrated water vapor increasing from 14 to 22 kg m^{-2} . Near the surface, temperatures remained close to 0°C , accompanied by persistent fog. For the following discussion of aerosol properties, the period from 15 to 22 July is defined as WA1, and that from 30 July to 3 August as WA2.

The two warm air mass regimes differed in their transport history and aerosol characteristics. Based on the backward trajectories shown in Fig. 3 and the surface-type influence (Fig. 4a), WA1 was associated with transport from the Eurasian sector towards the central Arctic, including substantial passage over the Barents Sea. In contrast, WA2 was characterized mainly by marine inflow from the North Atlantic and Nordic Seas, with comparatively limited continental influence before arrival at the ship position. These differences in transport pathways were reflected in the observed rBC properties and in the PM_{10} chemical composition (Fig. 5).

WA1 showed the highest BC enhancement among the central Arctic regimes. During this period, rBC mass

concentrations reached up to 74 ng m^{-3} , with a median value of $\sim 3.4 \text{ ng m}^{-3}$, while rBC number concentrations also increased relative to the preceding SE2 period ($N_{\text{rBC}} \sim 0.84 \text{ cm}^{-3}$, Fig. 4b–c). eBC concentrations were similarly enhanced and reached up to 111 ng m^{-3} . These enhanced values indicate that WA1 was associated with episodic transport of pollution into the central Arctic lower troposphere. WA1 is marked by strong continental outflow from Eurasia with strong passage over the Barents Sea towards the central Arctic. This Barents-sector pathway is widely regarded as the most effective corridor for carrying pollutants from northern Eurasian source regions into the Arctic (Stohl et al., 2013). A smaller subset of airmasses was also passing over the Norwegian Sea. In addition, the airmasses associated with WA1 were observed to affect regions known to contribute pollutants to the Arctic, particularly through gas flaring and metallurgical industrial sources (Stohl et al., 2013; Schulz et al., 2019; Dada et al., 2022). The trajectory analysis suggests that the airmasses sampled during WA1 had a stronger influence from lower-latitude source regions than those associated with the clean central Arctic regimes. In addition, the airmasses passed over regions with enhanced fire activity indicated by satellite fire-pixel data (confirmed by MODIS Visible Infrared Imaging Radiometer Suite (VIIRS) satellite data fire-pixel counts, as shown in Fig. S4). Along with this, we observed a significant increase in K^+ , which supports the predominant role of biomass burning influence during this period over the central Arctic. K^+ has been widely recognized as a good tracer for biomass burning in previous studies (Arun et al., 2019, 2021). The enhanced BC concentrations during WA1 demonstrate the importance of warm air mass intrusions as episodic pathways for transporting biomass burning aerosol into the Arctic marine boundary layer. Similar transport mechanisms have been reported previously for Arctic haze and intrusion events affecting the lower troposphere (Stohl et al., 2013; Schulz et al., 2019; Dada et al., 2022).

In contrast to WA1, WA2 was associated with a lower aerosol loading. During this period, rBC mass concentrations reached up to $\sim 35 \text{ ng m}^{-3}$, with a median of $\sim 1.6 \text{ ng m}^{-3}$, and the corresponding rBC number concentration $\sim 0.58 \text{ cm}^{-3}$. These values are elevated relative to the background regimes but remained clearly lower than those observed during WA1. WA2 was dominated mainly by marine inflow, and the chemical composition showed enhanced SO_4^{2-} and OC contributions relative to WA1. This suggests that WA2 reflected transport of more aged marine and regionally processed aerosol, with a weaker influence from direct combustion sources compared to WA1.

Earlier studies have shown that summertime Arctic rBC is generally characterized by very low background concentrations, with occasional enhancements linked to transport. Taketani et al. (2016) reported pronounced spatial variability between the North Pacific and Arctic oceans in September, with rBC mass concentrations ranging from 0 to 60 ng m^{-3}

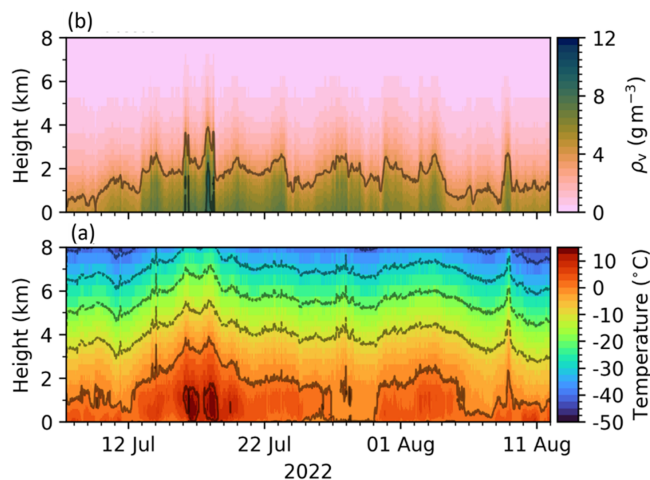


Figure 6. (a) HATPRO microwave radiometer retrieval of air temperature (K) vertical profiles, (b) absolute humidity from HATPRO.

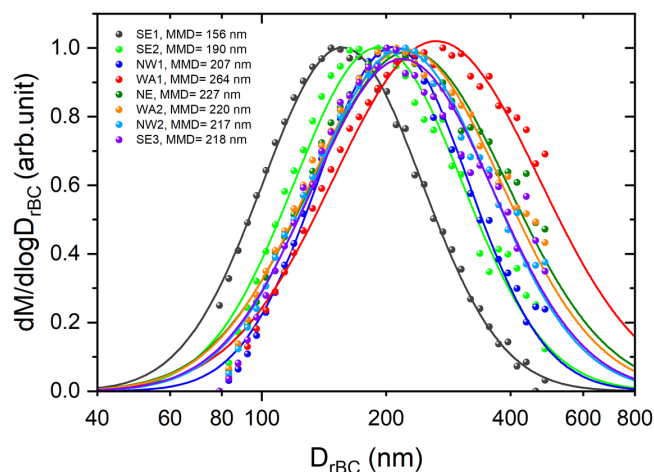


Figure 7. Mass size distribution of refractory black carbon particles estimated during the ATWAICE cruise during distinct airmass conditions. [TS4](#)

and an average of about 1 ng m^{-3} , while Schulz et al. (2019) observed that combustion particles constituted only a minor fraction of the aerosol population in the Canadian Arctic during summer, with near-surface rBC concentrations typically below 2 ng m^{-3} , reflecting weak exchange between the summer polar dome and mid-latitude airmasses. In the present study, most airmass regimes, including NW1, NW2, SE2, SE3, and NE, exhibited similarly low mean rBC concentrations of about $1.4\text{--}1.6 \text{ ng m}^{-3}$, with median values of $0.5\text{--}0.8 \text{ ng m}^{-3}$, indicating that these conditions represent the clean summertime Arctic background (AMAP, 2015; Zanatta et al., 2023; Jurányi et al., 2023). Our observed rBC concentrations are also lower than those reported by Liu et al. (2015) in the European Arctic during spring, where rBC mass concentrations ranged from 20 to 100 ng m^{-3} , as expected from the seasonal transition from the spring Arctic haze period to the comparatively cleaner summer atmosphere. At the same time, the two warm airmass intrusion cases demonstrate that episodic transport can still substantially perturb this otherwise low-rBC environment. These enhanced values are comparable to or approach those reported at Arctic receptor sites such as Pallas, Finland (26 ng m^{-3} ; Raatikainen et al., 2015) and Zeppelin, Svalbard ($39 \pm 23 \text{ ng m}^{-3}$; Zanatta et al., 2018), but remain far lower than those reported for marine and continental regions outside the Arctic, including the remote Atlantic Ocean ($\sim 100 \text{ ng m}^{-3}$) (Pan et al., 2026), south-eastern Arabian Sea ($938 \pm 293 \text{ ng m}^{-3}$), northern Indian Ocean ($546 \pm 80 \text{ ng m}^{-3}$), equatorial Indian Ocean ($206 \pm 114 \text{ ng m}^{-3}$) (Kompalli et al., 2021), Thumba ($670 \pm 571 \text{ ng m}^{-3}$; Nithin et al., 2026), Mukteshwar in the Himalayas ($1000 \pm 600 \text{ ng m}^{-3}$; Raatikainen et al., 2017), and Lulang on the Tibetan Plateau ($310 \pm 550 \text{ ng m}^{-3}$; Wang et al., 2018). The markedly enhanced BC levels during WA1 (eBC as high as 111 ng m^{-3} , rBC as high as 74 ng m^{-3}), while clearly elevated relative to background, remain lower

than the values observed during warm air-mass intrusions in spring (Dada et al., 2022), in subarctic environments, and in near-source high Arctic sites (Popovicheva et al., 2017). Table 1 summarizes our observed M_{rBC} values in comparison with those reported in previous studies from marine, remote, coastal environments.

3.3 Size distribution of refractory BC particles

Figure 7 shows the mass size distributions of rBC particles for the different airmass regimes during the cruise. The size distribution of rBC is relevant for interpreting its atmospheric processing and radiative effects, as the light absorption properties of BC depend on core size, while the observed mass median diameter (MMD) can be influenced by source characteristics as well as by aging and removal during transport (Shiraiwa et al., 2007; McMeeking et al., 2010; Liu et al., 2014; Taylor et al., 2014; Kompalli et al., 2020, 2021; Yang et al., 2025).

The estimated MMD varied substantially across the different transport regimes. During SE1, the MMD was $\sim 156 \text{ nm}$, i.e., the lowest among all regimes in this study. This value lies within the range commonly reported for polluted environments influenced by fossil fuel combustion, although such comparisons should be interpreted cautiously because the observed size distribution at the receptor site reflects not only source emissions but also atmospheric processing during transport (Laborde et al., 2013; Liu et al., 2019; Kompalli et al., 2020; Lim et al., 2023). As the ship moved away from the lower-latitudes towards the central Arctic, the MMD increased progressively; to $\sim 190 \text{ nm}$ during NW1, $\sim 207 \text{ nm}$ during SE2, and $\sim 225 \text{ nm}$ during NE. During NW2 and SE3, the MMD remained similarly larger, at $\sim 217 \text{ nm}$ and $\sim 218 \text{ nm}$, respectively. These observations of MMD indicate a systematic increase in rBC core size from the

Table 1. rBC mass concentration and mass median diameters reported in this study and the values available from previous studies in the marine, remote and coastal environments.

Location/Region	rBC mass concentration (ng m ⁻³)		Mass median diameter (nm)	Reference
	Mean ± SD	Median		
Marine environments				
South easterly 1	48.7 ± 49.8	36.8	156	Present study
North westerly 1	1.4 ± 3	0.6	207 ^{TS2}	Present study
North westerly 2	1.6 ± 2.5	0.8	217	Present study
South easterly 3	1.6 ± 3	0.8	218	Present study
South easterly 2	1.6 ± 3	0.5	190 ^{TS3}	Present study
North easterly	1.4 ± 2.7	0.6	227	Present study
Warm airmass intrusion 1	11 ± 14.4	3.4	264	Present study
Warm airmass intrusion 2	5.1 ± 8.3	1.6	220	Present study
Pallas, Finnish Arctic	26		161–231	Raatikainen et al. (2015)
Arctic Ocean	1 ± 1.2		~ 170	Taketani et al. (2016)
Zeppelin, Arctic	39 ± 23		240	Zanatta et al. (2018)
Alert	22 ± 13		160–180	Sharma et al. (2017)
Southern Ocean	0.14			Fossum et al. (2022)
South-eastern Arabian Sea	938 ± 293		190	Kompalli et al. (2021)
Northern Indian Ocean	546 ± 80		200	Kompalli et al. (2021)
Equatorial Indian Ocean	206 ± 114		190	Kompalli et al. (2021)
Remote Atlantic	100		180	Pan et al. (2026)
Remote environments				
Jungfrauoch, Switzerland	13.24	1.4–20.5	220–240	Liu et al. (2010)
Lulang, Tibetan Plateau, China	310 ± 550		160	Wang et al. (2018)
Mukteshwar, the Himalayas, India	1000 ± 600		205	Raatikainen et al. (2017)
North-eastern Qinghai–Tibetan Plateau, China	160 ± 190		187	Wang et al. (2015)
Melpitz	160		140	Yang et al. (2025)
Fukue Island Japan	160 ± 50		200–220	Shiraiwa et al. (2008)
Catalina Island	40 ± 10		153–170	Ko et al. (2020)
Coastal sites				
Thumba	670 ± 571		192	Nithin et al. (2026)
Mace Head	3.31			Fossum et al. (2022)

lower-latitudes towards the central Arctic regimes. However, this gradient should not be interpreted as a unique fingerprint of changing emission sources. In remote regions, rBC size distributions can be modified during transport by size-dependent removal and atmospheric processing, including cloud processing and coagulation (Pan et al., 2026). Therefore, in the absence of independent source-specific tracers and high-resolution chemical composition information, the increase in MMD towards higher latitudes is interpreted here as reflecting the combined effects of distinct sources and atmospheric processing rather than as direct evidence of a transition to a specific source type.

A pronounced enhancement in MMD was observed during the warm airmass intrusion regime WA1, for which the estimated MMD was higher than 260 nm. This value is substantially larger than those observed during the background

central Arctic regimes and coincided with enhanced rBC mass concentrations during the same period. As discussed in Sect. 3.2, WA1 was associated with transport from lower-latitude source regions along with the evidence for biomass burning influence. In contrast, during WA2, the MMD remained close to 220 nm, comparable to the values observed during the central Arctic background conditions. This difference between WA1 and WA2 further indicates that warm airmass intrusions into the central Arctic do not exert a uniform influence on the microphysical characteristics of rBC; rather, their effect on rBC size distribution depends on the transport pathways and the atmospheric processing within the advected airmass.

Changes in MMD during long-range atmospheric transport can arise from multiple competing processes. Size-dependent wet removal may preferentially remove larger BC

containing particles under some conditions and thereby shift the distribution towards smaller diameters (Moteki et al., 2012; Schulz et al., 2019). Conversely, coagulation and condensational aging may increase the apparent characteristic size of BC containing particles or preferentially preserve larger cores under specific transport conditions (Tunved et al., 2013; Schulz et al., 2019). The observed MMD thus reflects the combined influence of source emissions, removal, and atmospheric processing. This is particularly relevant in the Arctic, where transport pathways, cloud interactions, and scavenging processes jointly control the abundance and properties of BC reaching the central Arctic atmosphere (Liu et al., 2011; Schulz et al., 2019).

The MMD values observed during this campaign are within the broad range reported previously for Arctic and other remote environments, although substantial variability exists across regions and air mass transport regimes. In the present study, MMD ranged from ~ 156 nm during SE1 to ~ 264 nm during WA1, whereas the Arctic background regimes were characterized by MMD around 190–227 nm. These values are comparable to those reported for the Arctic Ocean in summer (~ 170 nm; Taketani et al. (2016), Pallas in the Finnish Arctic (161–231 nm; Raatikainen et al., 2015), and Zeppelin during spring (Zanatta et al., 2018), but are higher than the 119–134 nm reported for the high Canadian Arctic by Schulz et al. (2019). Previous studies from other remote and coastal environments similarly show a wide spread, including 140 nm at Melpitz (Yang et al., 2025), 153–170 nm at Catalina Island (Ko et al., 2020), 200–220 nm at Fukue Island (Shiraiwa et al., 2008), and ~ 192 nm at Thumba (Nithin et al., 2026). These comparisons indicate that the MMD values measured in this study are generally high relative to those reported for other marine/remote/coastal environments.

3.4 Mixing state of refractory BC containing particles

Figure 8 shows the size-resolved coating thickness of rBC particles estimated during the study period, along with the normalized rBC particle volume. The size resolved coating thickness (CT) of rBC particles, along with the number concentration of particles is given in Fig. S5. The size resolved CT classification provided a more direct insight into the mixing state of rBC particles in this study. It is evident that, throughout the study period, two distinct regions of rBC core sizes (below $D_c \sim 150$ nm and above $D_c \sim 150$ nm) consistently exhibited relatively higher volume of coated rBC. This suggests that the rBC population during the campaign exhibited pronounced mixing-state heterogeneity. The repeated occurrence of two enhanced-volume domains, one associated with smaller cores and another with larger cores, indicates that non-BC material was distributed unevenly across the rBC population, with some particles remaining weakly processed while others acquired substantial coatings. This particle-to-particle variability is important because the radiative effects of rBC depends not only on the mean coating

thickness but also on how the coating is distributed among particles of different core sizes, as emphasized in recent studies (Fierce et al., 2016, 2020; Zeng et al., 2024; Zhai et al., 2022).

The higher contribution from coated larger rBC cores under the northerly and near-pristine regimes likely reflects aged, internally mixed particles that underwent substantial atmospheric processing during long-range transport to the central Arctic. In this study, we found the relatively higher coated volume observed at both smaller and larger cores during SE2 and WA1 points to a broader spread of core-shell combinations, implying a more diverse and complex mixing state under those regimes in the Arctic. Such a pattern suggests that, in addition to aged large-core particles, a greater fraction of smaller rBC cores had also acquired sufficient condensed material to become internally mixed. Condensational aging generally enhances coating accumulation more efficiently on smaller BC cores than on larger ones (Seinfeld and Pandis, 2006). The bottom-left region with null values corresponds to smaller rBC particles that show neither positive nor negative coating thickness (CT), due to the detection limitations of the SP2, as reported in several studies (Ko et al., 2020; Yang et al., 2025). This detection limitation restricts the retrieval of coating information from scattered light for smaller rBC particles. As a result, the mixing state information of a substantial portion of these smaller rBC particles remains unresolved. This missing fraction of CT results in overestimation of CT when estimating the absolute coating thickness across the entire size range.

In order to provide a statistical insight into the mixing state information of rBC particles, the frequency distribution of CT estimated in the 180–300 nm is shown in Figure 9. The median CT for the near pristine, pristine and warm air mass conditions during the study ranged from 14–18, 9–20 and 12–15 nm respectively. It is found that coating thickness was relatively higher in regions influenced mainly by northerly air mass advectons (NE, NW1 and NW2, with $CT_{\text{median}} \sim 20$ nm, $CT_{\text{median}} \sim 18$ nm, and $CT_{\text{median}} \sim 18$ nm respectively), while the lowest coating thickness is found during SE2 ($CT_{\text{median}} \sim 9$ nm). In northerly air mass regimes, air masses likely experienced prolonged atmospheric residence times and active secondary aerosol condensation, leading to more internally mixed, coated rBC particles. Specifically for the northerly air masses, we observed a higher fractional contribution to the total aerosol mass from SO_4^{2-} , $\sim 18\%$ and OC $\sim 48\%$ especially during NE. The prolonged transport through marine and sea ice covered environments (Fig. 4a) and the associated extended atmospheric aging of rBC particles during NE could have facilitated the condensation of secondary species onto rBC cores. However, for the NW2, particularly when the ship was located in the Greenland Sea, the contributions from SO_4^{2-} and OC were even higher. These increased fractions of organics and sulfate may have contributed significantly to the observed enhancement in the coating of rBC cores during this pe-

riod. It is important to note that the NE regime was predominantly influenced by air masses traversing oceanic and sea-ice-covered regions, whereas the NW2 regime was more strongly affected by continental outflow from Greenland.

5 However, since simultaneous real-time submicron aerosol chemical composition measurements are not available alongside rBC data, we cannot definitively attribute the enhanced coating to these chemical species. Furthermore, the PM_{10} chemical composition discussed above reflects bulk aerosol
10 composition integrated over a 24 h period and across a broad size range, its relationship to SP2-derived submicron rBC coating thickness is qualitative; therefore, sulfate and OC fractions should not be interpreted as quantitative indicators of rBC coating.

15 During WA1, the median CT is ~ 12 nm. This suggests that warm air mass intrusions have a notable influence on the coating of rBC particles, as evidenced by the difference in CT between SE2 (prior to the warm air mass intrusion) and WA1. This difference could be attributed to the presence of
20 aged rBC particles transported into the central Arctic during these intrusions from biomass-burning sources, as discussed before. During WA2, as the ship re-entered the marginal ice zone, it was influenced by a warm air mass advection from the southeast, which primarily passed over oceanic regions. The
25 estimated median CT during this period is ~ 15 nm. Interestingly, during the second warm air mass intrusion, the prevailing air masses shifted from north-easterly to south-easterly, which could have contributed to the observed changes in coating thickness. CT, along with a relatively higher contribution of air masses traversing open oceanic regions, suggests relatively aged rBC particles during WA2. This could have significantly influenced the observed changes in CT between WA2 and WA1, where continental emissions and biomass-burning sources were more prominent. In addition,
35 we noticed that the mass fractions of SO_4^{2-} , NH_4^+ , MSA, and $C_2O_4^{2-}$ were higher during WA2 than during WA1. Further, we found significant correlations between NH_4^+ and SO_4^{2-} ($R^2 = 0.5$), SO_4^{2-} and MSA ($R^2 = 0.4$), $C_2O_4^{2-}$ and NO_3^- ($R^2 = 0.6$), suggesting enhanced secondary aerosol formation/photochemical aging during this period. Consistent with this, Arun et al. (2021; and references therein) reported substantial organic aerosol formation and photochemical aging in a remote environment over the eastern Himalayas. These findings further support the aged nature of the aerosols during WA2, which likely contributed to the relatively high CT during WA2.

Despite evidence of long-range transport, rBC particles in this study showed thin to moderate coatings, unlike previous observations in background environments with thickly coated rBC particles (Motos et al., 2020; Yang et al., 2025; Pan et al., 2026). This infers lower precursor gas concentrations and limited condensation under summer Arctic conditions, where clean background air and reduced SOA formation can suppress coating even on aged rBC particles.

Additionally, in-cloud and below-cloud scavenging, especially during the prevalent fog and low-level cloud conditions of Arctic summer, likely play a significant role in removing hydrophilic or heavily coated rBC particles. The persistent presence of clouds and fog enhances wet scavenging, which significantly influence the rBC properties. This effect is particularly evident in our observations from warm air mass intrusions (WA1), which, despite being associated with biomass burning and continental sources, showed significantly larger rBC cores (MMD > 260 nm) but surprisingly thinner coatings than background air masses, such as those from the NE and NW sectors. These background regimes, dominated by air masses traversing marine or consolidated sea-ice regions, featured moderately large rBC cores (MMD ~ 220 nm) with moderate coatings, suggesting the combined influence of aerosol aging and active wet scavenging. The lower coating thickness observed in the southeast sectors (e.g., SE2), despite large MMDs, indicate that particle aging alone does not necessarily lead to thicker coatings; rather, prevailing environmental conditions, such as low oxidant levels or cleaner marine air masses, can suppress formation of coating on rBC particles. Coating thickness may also be modulated by the available condensation sink. Under high particle number conditions, condensable material can be distributed across a larger population, potentially limiting per-particle coating growth even when precursors are present. Although we cannot quantify this effect here because SP2 number concentrations represent only BC-containing particles within the instrument's detection range (and not the full aerosol population), this mechanism could also contribute to the relatively low CT observed during high loading regimes such as WA1.

3.5 Light absorption enhancement of rBC particles

To understand the role of microphysical properties and mixing state in modulating BC light absorption, we quantified the light absorption enhancement (E_{abs}) and mass absorption cross-section (MAC) of rBC particles using core-shell Mie theory, constrained by our in-situ single-particle observations obtained using SP2 as described in Sect. 2.2. In this method, E_{abs} represents the increase in light absorption by coated rBC relative to uncoated (bare) BC, while MAC provides the corresponding absorption efficiency per unit rBC mass. For smaller core sizes, even modest coatings can result in substantial enhancement due to the strong lensing effect. However, as the core size increases, the relative impact of coatings on absorption enhancement diminishes. Figure S6 shows the size-resolved E_{abs} and MAC of rBC particles across the different air mass regimes. In the following discussion, we focus on the ranges defined by the 80–500 and 180–300 nm core size intervals. The size range 80 to 500 nm indicates the upper limit of E_{abs} and MAC, possibly overestimated due to the missing part of mixing state information in the lower size ranges as discussed. Similarly, the 180–300 nm size range

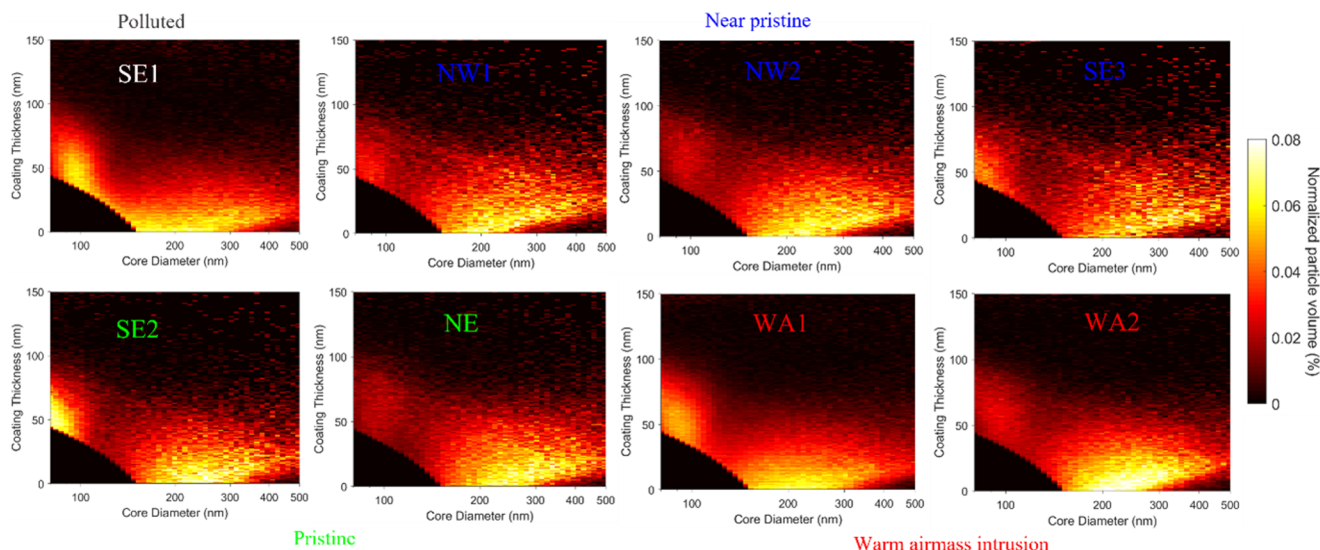


Figure 8. Size resolved coating thickness of rBC particles during the campaign. The colour bar indicates the particle volume normalized with the integrated total volume (in %) in each size bin.

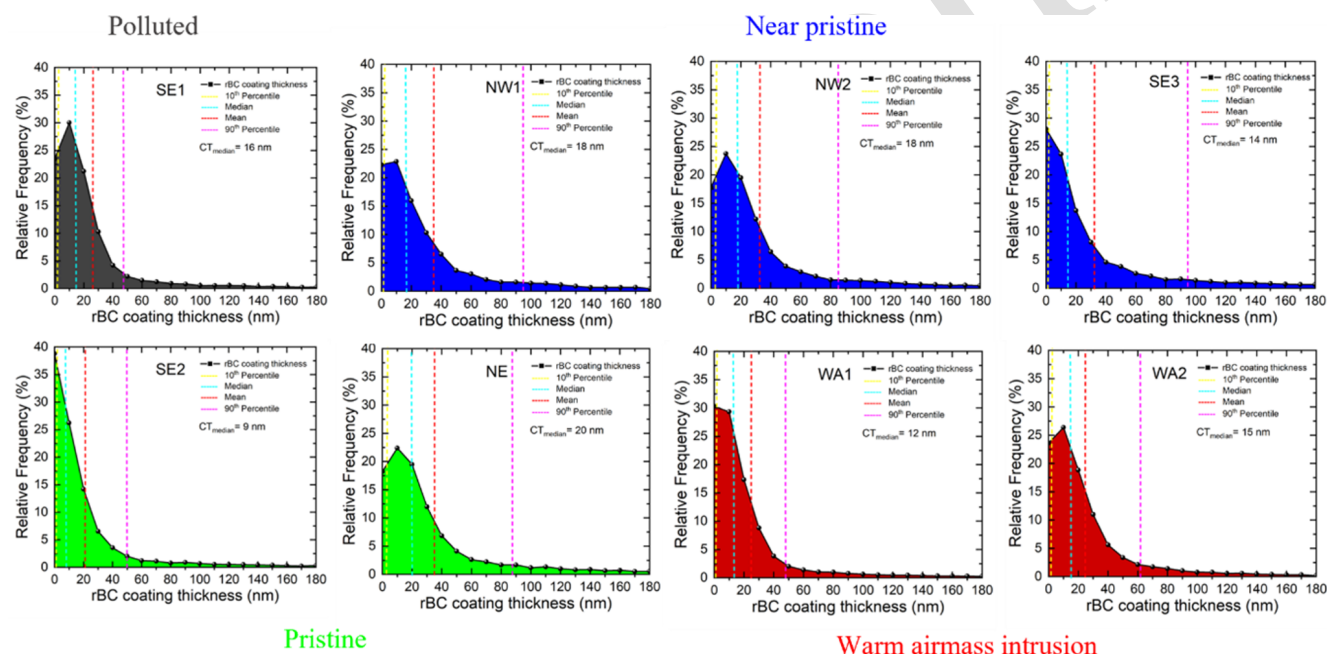


Figure 9. Frequency distribution of the coating thickness histograms during the study period for each airmass regimes for the rBC core size range of 180–300 nm.

corresponds to the lower range of E_{abs} and MAC values in this study. The size-resolved E_{abs} values ranged from approximately 1.0 to 1.6 during the study period (Fig. 10). During the polluted initial phase of the campaign, when the sampled airmasses were influenced predominantly by continental and anthropogenically processed sources, E_{abs} ranged from ~ 1.1 to 1.4 (Fig. 10a), with corresponding MAC values of ~ 6.6 – $8.0 \text{ m}^2 \text{ g}^{-1}$ (Fig. 10b). These MAC values are comparable to those reported for anthropogenically influ-

enced environments, including $\sim 6.5 \text{ m}^2 \text{ g}^{-1}$ in South China, $\sim 7.5 \text{ m}^2 \text{ g}^{-1}$ in California, $\sim 8.4 \text{ m}^2 \text{ g}^{-1}$ in Karlsruhe, and $\sim 7.0 \text{ m}^2 \text{ g}^{-1}$ during ACE-Asia flight measurements (Lan et al., 2013; Cappa et al., 2019; Linke et al., 2016; Clarke et al., 2004), indicating moderate absorption enhancement under polluted conditions. They are, however, lower than values reported for the regions such as ~ 9.5 – $10.4 \text{ m}^2 \text{ g}^{-1}$ at Nordic background sites, $\sim 11.8 \text{ m}^2 \text{ g}^{-1}$ in Nanjing, and

$\sim 12.3 \text{ m}^2 \text{ g}^{-1}$ at Jeju Island (Zanatta et al., 2016; Ma et al., 2020; Kondo et al., 2009).

Interestingly, during WA1, despite the predominant influence of biomass-burning emissions, both E_{abs} ($\sim 1.0\text{--}1.2$) and MAC ($\sim 6.5\text{--}8.0 \text{ m}^2 \text{ g}^{-1}$) remained relatively low, even lower than those observed under pristine/background Arctic conditions ($E_{\text{abs}} \sim 1.1\text{--}1.6$; MAC $\sim 6.5\text{--}8.7 \text{ m}^2 \text{ g}^{-1}$). This is notable because biomass-burning-influenced aerosols often exhibit substantially stronger absorption enhancement and higher MAC after atmospheric aging. For example, previous studies have reported E_{abs} values of ~ 1.38 during biomass-burning events in Boulder, ~ 1.5 in the Pearl River Delta, and synthesis-based values of ~ 1.83 for biomass-burning smoke globally (Lack et al., 2012; Wu et al., 2018; Asmi et al., 2025). Similarly, MAC values of $\sim 13.3 \text{ m}^2 \text{ g}^{-1}$ in Texas biomass-burning plumes and a global mean of $\sim 14.7 \text{ m}^2 \text{ g}^{-1}$ for biomass-burning conditions are considerably higher than those observed here (Schwarz et al., 2008; Asmi et al., 2025). Although reduced coating thickness during WA1 is consistent with lower absorption enhancement, caution should be taken against interpreting WA1 as being controlled solely by a limited coating to low E_{abs} mechanism. For Arctic transport events, the observed E_{abs} likely reflects a combination of constrained atmospheric processing (limited aging and coating) and source-related differences in rBC properties. In particular, differences in rBC composition, morphology/internal structure, and particle scale mixing heterogeneity can reduce absorption efficiency and/or make core-shell Mie-based representations less effective or less representative.

In contrast, WA2 exhibited somewhat higher enhancement, with E_{abs} increasing to $\sim 1.1\text{--}1.5$, indicating more extensive atmospheric processing and thicker coatings acquired during long-range transport. Such aging likely promoted condensation of secondary species and enhanced internal mixing, thereby increasing absorption via the lensing effect. The higher E_{abs} during WA2 compared with WA1 suggests that the radiative effects of rBC in the central Arctic depend not only on source type, but also strongly on the extent of atmospheric processing during transport. In this context, coating thickness (CT) serves as an important proxy for particle aging and internal mixing state, both of which directly modulate absorption enhancement. The contrast between WA1 and WA2 therefore highlights the importance of size-resolved coating information for interpreting variability in rBC optical properties across different air mass regimes.

It is worth noting that the estimated E_{abs} values in this study are comparable with earlier field observations, including ~ 1.06 in California (Cappa et al., 2012), ~ 1.06 at an east Asian outflow site Noto Peninsula (Ueda et al., 2016), ~ 1.38 during biomass burning events in Boulder (Lack et al., 2012), 1.50 ± 0.48 in the Pearl River Delta (Wu et al., 2018), ~ 1.36 for marine air mass periods to ~ 1.58 for the continental air mass periods over a tropical coastal site (Nithin et al., 2026), ~ 1.15 in Beijing (Liu et al., 2020), and ~ 1.69 in Shanghai (Zhai et al., 2022), ~ 1.42 Nanjing

in China (Ma et al., 2020), $1.1\text{--}1.3$ in a background site in the Qinghai-Tibet Plateau (Zeng et al., 2024). Larger values approaching or exceeding 2 have been observed in strongly aged or biomass-burning-influenced aerosol, such as pyrocumulonimbus plumes and remote high-altitude environments (Beeler et al., 2024; Tinorua et al., 2024). Zhang et al. (2023) also reported E_{abs} in the range of $\sim 1.2\text{--}2.0$ with higher E_{abs} for fully coated BC in North China Plain. Utilizing the global measurements, Asmi et al. (2025; and references therein) reported average E_{abs} for the urban and remote environments as 1.38 and 1.59 respectively as well as $E_{\text{abs}} \sim 1.8\text{--}3.0$ for the biomass burning smoke. Laboratory evidence also indicates that coatings can substantially enhance BC absorption. Shiraiwa et al. (2010) found an approximately 2-fold increase in absorption for BC coated with oleic acid and glycerol, while Khalizov et al. (2009) reported an E_{abs} of around 1.4 after sulfuric acid condensation on black carbon. These previous studies collectively indicate that most atmospheric E_{abs} values fall in the range of about $1.0\text{--}2.0$ under typical ambient conditions, while higher values are generally associated with extensive aging, thicker coatings, or biomass-burning influence. It is important to note, however, that E_{abs} values reported in the literature are derived using different methodological approaches, including core-shell Mie theory, thermogravimetric coupled with photoacoustic absorption measurements, filter-based methods, and optical approaches combining cavity ring-down spectroscopy and nephelometry. Similarly, MAC values have been derived using different combinations of absorption measurements and BC mass quantification, such as PSAP or photoacoustic absorption together with EC, SP2, SP-AMS, or COSMOS measurements. These methodological differences can contribute to inter-study variability and should be considered when comparing absolute values across regions and source regimes. Tables S1 and S2 in the Supplement providing an overview of the E_{abs} and MAC values and methods used in previous studies in comparison with our observations. It is important to note that the E_{abs} values reported here are based on a core-shell Mie theory that assumes a spherical BC core fully encapsulated by non-absorbing coating material. Ambient rBC particles, however, often exhibit fractal/irregular morphologies, partial coating, and mixing state heterogeneity. As a result, core-shell-based E_{abs} may represent an upper-bound or idealized estimate of absorption enhancement relative to more realistic particle representations (e.g., Adachi et al., 2010; Ueda et al., 2016; Fierce et al., 2020; Liu et al., 2020; Zhai et al., 2022; Romshoo et al., 2024). Overall, the present results indicate that most E_{abs} values in the central Arctic fall within the lower to moderate range reported for ambient atmospheric conditions, and that the variability between regimes is primarily controlled by the combined influence of source characteristics, atmospheric aging, removal processes and mixing state.

The size-resolved variation in E_{abs} , MAC, and coating thickness across different air masses have critical implica-

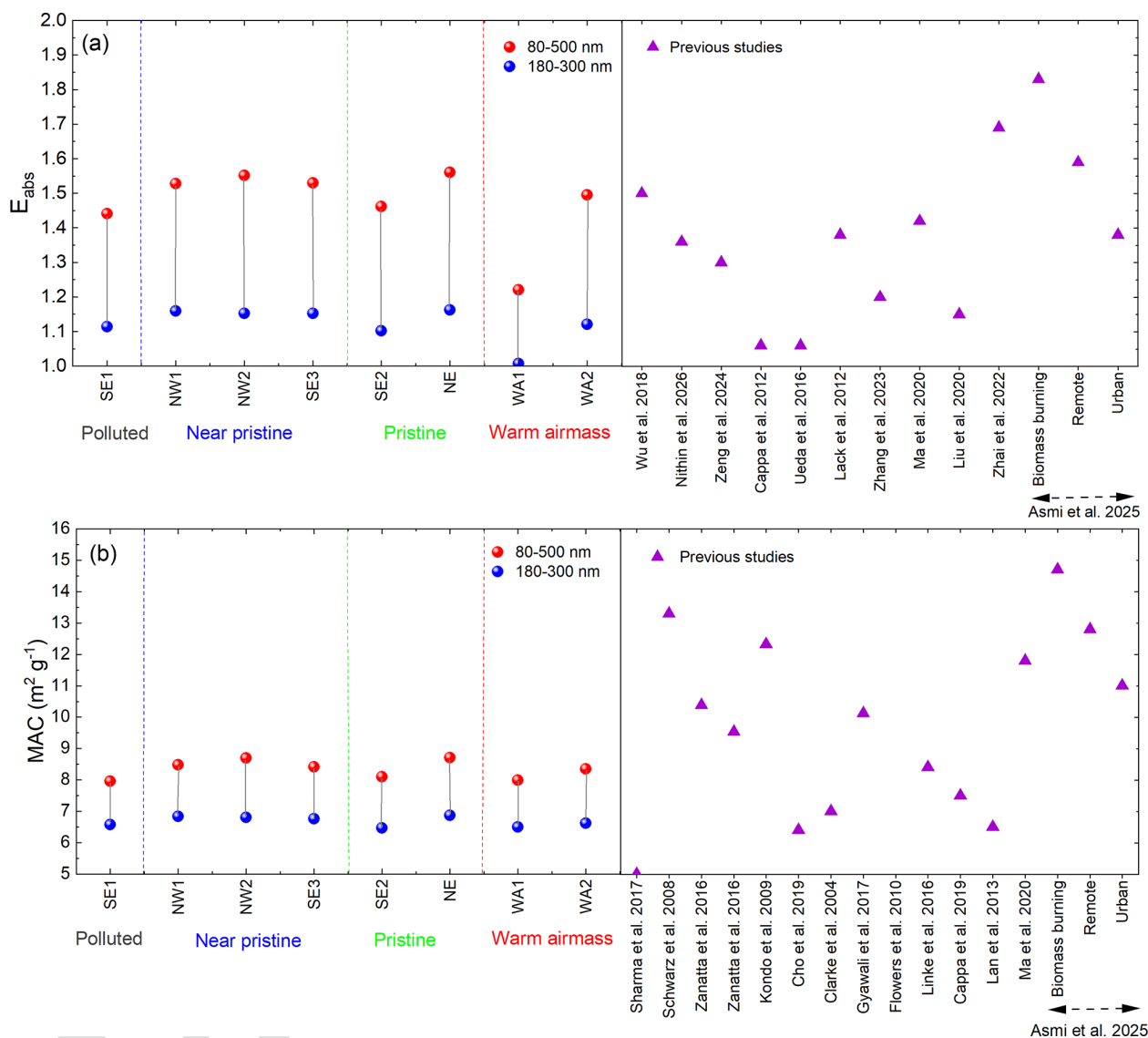


Figure 10. (a) Estimated absorption enhancement (E_{abs}) and of refractory black carbon particles for each regime for the rBC core size ranges, 80–500 and 180–300 nm. (b) Estimated mass absorption cross section of refractory black carbon particles for each regime for the rBC core size ranges, 80–500 and 180–300 nm. [TSS](#)

tions for understanding the radiative impacts of BC in the Arctic. Highly coated BC particles can significantly increase shortwave radiation absorption, contributing to local atmospheric warming and potential feedbacks through snow and sea-ice albedo reduction. The pronounced absorption enhancement observed during WA1 suggests that continental or anthropogenically influenced airmasses, though less frequent, can be major contributors to BC radiative forcing in the Arctic MBL. Nonetheless, several limitations should be acknowledged. Mie theory, used for estimating E_{abs} , assumes spherical core-shell morphology, which may not accurately capture the irregular or fractal shapes of ambient BC aggregates, particularly in fresh emissions. The observed heterogeneity in rBC optical properties across airmass regimes un-

derscore the need for dynamic, region-specific parameterizations in climate models. Relying on constant enhancement factors or bulk MAC values across different transport conditions risks oversimplifying the real variability. It could lead to significant uncertainties in estimates of BC direct radiative forcing. These findings provide essential observational constraints for climate models and underscore the need to incorporate rBC mixing state and size-resolved properties into Arctic radiative effect assessments.

4 Conclusions

To investigate the microphysical properties and mixing state of atmospheric refractory black carbon (rBC) particles in the

central Arctic marine boundary layer, measurements were conducted on board RV *Polarstern* during the ATWAICE campaign in summer 2022. This study provides new insights into the spatial and temporal variability of rBC properties including its abundance, size distribution, mixing state, and radiative properties during the summer melt season. Our results reveal that airmass transport pathways, atmospheric processing and removal mechanisms strongly influence rBC abundance, its size distribution, and mixing state in the summertime central Arctic marine boundary layer. rBC mass concentrations, size distributions, and coating thickness varied substantially across the different transport regimes considered in this study. The lowest rBC mass concentrations were observed under pristine and near-pristine conditions, typically on the order of $\sim 0.4\text{--}0.6\text{ ng m}^{-3}$. In contrast warm airmass intrusions into the central Arctic were associated with clear enhancements in rBC, with maximum concentrations reaching $\sim 74\text{ ng m}^{-3}$ during WA1. These results demonstrate that episodic transport from lower latitudes can strongly perturb the otherwise low-aerosol summertime Arctic background. Further, the higher rBC during WA1 is found to be associated with significant influences from the biomass burning sources during the warm airmass intrusion.

The mass median diameter (MMD) of rBC varied substantially across the different transport regimes with a clear latitudinal shift in the mass median diameter (MMD) of rBC from the lower latitude near coastal marine environments ($\sim 156\text{ nm}$) to the high latitudes of the central Arctic ($\sim 220\text{ nm}$). The particularly high MMD observed during WA1 ($> 260\text{ nm}$) indicates that warm-air intrusions can substantially modify the microphysical properties of rBC in the central Arctic. The observed variability in MMD is interpreted as reflecting the combined effects of source influence, airmass transport pathways, and atmospheric processing during long-range transport, rather than a unique signature of emission source alone. The mixing state of rBC showed similarly strong regime dependence. The size-resolved mixing state revealed pronounced heterogeneity, with non-BC material distributed unevenly across rBC particles of different core sizes. Airmasses with higher continental influence generally exhibited enhanced rBC concentrations and distinct coating characteristics relative to the clean marine and sea-ice influenced regimes. At the same time, the observed coating thickness were often lower than that might be expected for aged particles transported over long distances.

The size-resolved analysis of light absorption properties based on the core-shell Mie theory further showed substantial variability in both the absorption enhancement (E_{abs}) and the mass absorption cross-section (MAC). The size-resolved E_{abs} values ranged from approximately 1.0–1.6 across all airmass regimes. The pristine and near-pristine regimes exhibited comparatively high E_{abs} and MAC values, consistent with more internally mixed and atmospherically processed particles. In contrast, WA1 showed comparatively low E_{abs} (generally < 1.1) despite enhanced rBC concentrations, indi-

cating that the particles transported during this event were not necessarily highly coated. By comparison, WA2 exhibited higher E_{abs} than WA1, with weaker evidence of direct combustion influence. This contrast indicates that the radiative properties of rBC in the Arctic are governed not only by source region but also by airmass transport pathways, as passage over marine or relatively cleaner environments may promote prolonged aging and a greater influence of secondarily processed aerosol on the mixing state of rBC. The results emphasize that fixed or generalized MAC or E_{abs} are unlikely to adequately represent Arctic conditions. Instead, regime-specific and size-resolved representations that account for mixing state and atmospheric aging conditions are needed to improve model descriptions of BC radiative effects in the Arctic. Given the high climatic sensitivity of the Arctic to light absorbing aerosols perturbations, improved characterization of rBC abundance, size and mixing state heterogeneity is essential for reducing uncertainties in estimates of aerosol radiative forcing and Arctic climate projections.

Data availability. Data are available upon request from the corresponding author (arun.babu@tropos.de).

Supplement. The supplement related to this article is available online at [the link will be implemented upon publication]. [TS6](#)

Author contributions. BSA, TM, MLP, BW conceptualized the study. BSA, SL, PO conducted onboard measurements. BSA, TM, MvP performed data processing. AW, JR provided the radiometer datasets. BSA prepared the original draft of the paper. All authors contributed to reviewing and editing the manuscript.

Competing interests. At least one of the (co-)authors is a member of the editorial board of *Atmospheric Chemistry and Physics*. The peer-review process was guided by an independent editor, and the authors also have no other competing interests to declare.

Disclaimer. Publisher's note: Copernicus Publications remains neutral with regard to jurisdictional claims made in the text, published maps, institutional affiliations, or any other geographical representation in this paper. The authors bear the ultimate responsibility for providing appropriate place names. Views expressed in the text are those of the authors and do not necessarily reflect the views of the publisher.

Acknowledgements. We gratefully acknowledge the funding by the German Research Foundation, DFG grants WE 2757/6-1 and HE 5214/10-1. We gratefully acknowledge the support by Deutsche Forschungsgemeinschaft through the Transregional Collaborative Research Centre TRR-172 "Arctic Amplification: Climate Relevant Atmospheric and Surface Processes, and Feedback Mecha-

nisms (AC)^{3m} (grant 268020496). We thank Heike Wex and Holger Siebert (Leibniz Institute for Tropospheric Research, Germany) for the helpful suggestions and comments on improving this paper. We also thank Dr. Bruna A. Holanda (Hessian Agency for Nature Conservation, Environment and Geology, Germany) for her support during this study. We thank everyone involved in the expedition of the research vessel *Polarstern* during ATWAICE in 2022 (Grant No. AWI_PS131_11 (Alfred-Wegener-Institut Helmholtz-Zentrum für Polar-und Meeresforschung, 2017)). We thank the Institute of Environmental Physics, University of Bremen, for the provision of the merged MODIS-AMSR2 sea-ice concentration data at https://data.seaice.uni-bremen.de/modis_amsr2 (last access: 15 October 2023). We acknowledge the use of Grammarly during the preparation of this paper. We thank Torsten Kanzow and the ATWAICE team for their support during the campaign.

Financial support. This research has been supported by the Deutsche Forschungsgemeinschaft (grant no. WE 2757/6-1 and HE 5214/10-1).

Review statement. This paper was edited by Manabu Shiraiwa and reviewed by Sayako Ueda and one anonymous referee.

References

- Adachi, K., Chung, S. H., and Buseck, P. R.: Shapes of soot aerosol particles and implications for their effects on climate, *J. Geophys. Res.-Atmos.*, 115, <https://doi.org/10.1029/2009JD012868>, 2010.
- AMAP: AMAP Assessment 2015: Black carbon and ozone as Arctic climate forcers, Arctic Monitoring and Assessment Programme (AMAP), Oslo, Norway, 116 pp., ISBN 978-82-7971-092-9, 2015.
- Arun, B. S., Aswini, A. R., Gogoi, M. M., Hegde, P., Kumar Kompalli, S., Sharma, P., and Suresh Babu, S.: Physico-chemical and optical properties of aerosols at a background site (~4 km a.s.l.) in the western Himalayas, *Atmos. Environ.*, 218, <https://doi.org/10.1016/j.atmosenv.2019.117017>, 2019.
- Arun, B. S., Gogoi, M. M., Hegde, P., Borgohain, A., Boreddy, S. K. R., Kundu, S. S., and Babu, S. S.: Carbonaceous Aerosols over Lachung in the Eastern Himalayas: Primary Sources and Secondary Formation of Organic Aerosols in a Remote High-Altitude Environment, *ACS Earth Space Chem.*, 5, 2493–2506, <https://doi.org/10.1021/acsearthspacechem.1c00190>, 2021.
- Asmi, E., Backman, J., Servomaa, H., Virkkula, A., Gini, M. I., Eleftheriadis, K., Müller, T., Ohata, S., Kondo, Y., and Hyvärinen, A.: Absorption instruments inter-comparison campaign at the Arctic Pallas station, *Atmos. Meas. Tech.*, 14, 5397–5413, <https://doi.org/10.5194/amt-14-5397-2021>, 2021.
- Asmi, E., Sipkens, T. A., Saturno, J., Backman, J., Vasilatou, K., Weingartner, E., Keller, A., Ciupek, K., Müller, T., Babu Suja, A., Močnik, G., Drinovec, L., Eleftheriadis, K., Gini, M. I., Nowak, A., and Corbin, J. C.: Mass absorption cross-section of ambient black carbon aerosols – a review, *NPJ Clim. Atmos. Sci.*, <https://doi.org/10.1038/s41612-025-01288-2>, 2025.
- Backman, J., Schmeisser, L., Virkkula, A., Ogren, J. A., Asmi, E., Starkweather, S., Sharma, S., Eleftheriadis, K., Uttal, T., Jeffer-
son, A., Bergin, M., Makshtas, A., Tunved, P., and Fiebig, M.: On Aethalometer measurement uncertainties and an instrument correction factor for the Arctic, *Atmos. Meas. Tech.*, 10, 5039–5062, <https://doi.org/10.5194/amt-10-5039-2017>, 2017.
- Baumgardner, D., Popovicheva, O., Allan, J., Bernardoni, V., Cao, J., Cavalli, F., Cozic, J., Diapouli, E., Eleftheriadis, K., Genberg, P. J., Gonzalez, C., Gysel, M., John, A., Kirchstetter, T. W., Kuhlbusch, T. A. J., Laborde, M., Lack, D., Müller, T., Niessner, R., Petzold, A., Piazzalunga, A., Putaud, J. P., Schwarz, J., Sheridan, P., Subramanian, R., Swietlicki, E., Valli, G., Vecchi, R., and Viana, M.: Soot reference materials for instrument calibration and intercomparisons: a workshop summary with recommendations, *Atmos. Meas. Tech.*, 5, 1869–1887, <https://doi.org/10.5194/amt-5-1869-2012>, 2012.
- Beeler, P., Kumar, J., Schwarz, J. P., Adachi, K., Fierce, L., Per-ring, A. E., Katich, J. M., and Chakrabarty, R. K.: Light absorption enhancement of black carbon in a pyrocumulonimbus cloud, *Nat. Commun.*, 15, <https://doi.org/10.1038/s41467-024-50070-0>, 2024.
- Beer, E., Eisenman, I., and Wagner, T. J. W.: Polar Amplification Due to Enhanced Heat Flux Across the Halocline, *Geophys. Res. Lett.*, 47, <https://doi.org/10.1029/2019GL086706>, 2020.
- Birch, M. E. and Cary, R. A.: Elemental Carbon-Based Method for Monitoring Occupational Exposures to Particulate Diesel Exhaust, *Aerosol Sci. Tech.*, 25, 221–241, <https://doi.org/10.1080/02786829608965393>, 1996.
- Bohren, C. F. and Huffman, D. R.: *Frontmatter*, in: *Absorption and Scattering of Light by Small Particles*, Wiley, <https://doi.org/10.1002/9783527618156.fmatter>, 1998.
- Bond, T. C., Doherty, S. J., Fahey, D. W., Forster, P. M., Berntsen, T., Deangelo, B. J., Flanner, M. G., Ghan, S., Kärcher, B., Koch, D., Kinne, S., Kondo, Y., Quinn, P. K., Sarofim, M. C., Schultz, M. G., Schulz, M., Venkataraman, C., Zhang, H., Zhang, S., Bellouin, N., Guttikunda, S. K., Hopke, P. K., Jacobson, M. Z., Kaiser, J. W., Klimont, Z., Lohmann, U., Schwarz, J. P., Shindell, D., Storelvmo, T., Warren, S. G., and Zender, C. S.: Bounding the role of black carbon in the climate system: A scientific assessment, *J. Geophys. Res.-Atmos.*, 118, 5380–5552, <https://doi.org/10.1002/jgrd.50171>, 2013.
- Bozem, H., Hoor, P., Kunkel, D., Köllner, F., Schneider, J., Herber, A., Schulz, H., Leaitch, W. R., Aliabadi, A. A., Willis, M. D., Burkart, J., and Abbatt, J. P. D.: Characterization of transport regimes and the polar dome during Arctic spring and summer using in situ aircraft measurements, *Atmos. Chem. Phys.*, 19, 15049–15071, <https://doi.org/10.5194/acp-19-15049-2019>, 2019.
- Cappa, C. D., Onasch, T. B., Massoli, P., Worsnop, D. R., Bates, T. S., Cross, E. S., Davidovits, P., Hakala, J., Hayden, K. L., Jobson, B. T., Kolesar, K. R., Lack, D. A., Lerner, B. M., Li, S. M., Mellon, D., Nuaaman, I., Olfert, J. S., Petäjä, T., Quinn, P. K., Song, C., Subramanian, R., Williams, E. J., and Zaveri, R. A.: Radiative absorption enhancements due to the mixing state of atmospheric black carbon, *Science*, 337, 1078–1081, <https://doi.org/10.1126/science.1223447>, 2012.
- Cappa, C. D., Zhang, X., Russell, L. M., Collier, S., Lee, A. K. Y., Chen, C.-L., Betha, R., Chen, S., Liu, J., Price, D. J., Sanchez, K. J., McMeeking, G. R., Williams, L. R., Onasch, T. B., Worsnop, D. R., Abbatt, J., and Zhang, Q.: Light absorption by ambient black and brown carbon and its dependence

- on black carbon coating state for two California, USA, cities in winter and summer, *J. Geophys. Res.-Atmos.*, 124, 1550–1577, <https://doi.org/10.1029/2018JD029501>, 2019.
- Ching, J., Riemer, N., and West, M.: Black carbon mixing state impacts on cloud microphysical properties: Effects of aerosol plume and environmental conditions, *J. Geophys. Res.*, 121, 5990–6013, <https://doi.org/10.1002/2016JD024851>, 2016.
- Ching, J., West, M., and Riemer, N.: Quantifying impacts of aerosol mixing state on nucleation-scavenging of black carbon aerosol particles, *Atmosphere*, 9, <https://doi.org/10.3390/atmos9010017>, 2018.
- Cho, C., Kim, S. W., Lee, M., Lim, S., Fang, W., Gustafsson, Ö., Andersson, A., Park, R. J., and Sheridan, P. J.: Observation-based estimates of the mass absorption cross-section of black and brown carbon and their contribution to aerosol light absorption in East Asia, *Atmos. Environ.*, 212, 65–74, <https://doi.org/10.1016/j.atmosenv.2019.05.024>, 2019.
- Clarke, A. D., Shinzuka, Y., Kapustin, V. N., Howell, S., Huebert, B., Doherty, S., Anderson, T., Covert, D., Anderson, J., Hua, X., Moore, K. G., McNaughton, C., Carmichael, G., and Weber, R.: Size distributions and mixtures of dust and black carbon aerosol in Asian outflow: Physicochemistry and optical properties, *J. Geophys. Res.-Atmos.*, 109, <https://doi.org/10.1029/2003JD004378>, 2004.
- Croft, B., Martin, R. V., Leaitch, W. R., Tunved, P., Breider, T. J., D’Andrea, S. D., and Pierce, J. R.: Processes controlling the annual cycle of Arctic aerosol number and size distributions, *Atmos. Chem. Phys.*, 16, 3665–3682, <https://doi.org/10.5194/acp-16-3665-2016>, 2016.
- Dada, L., Angot, H., Beck, I., Baccarini, A., Quéléver, L. L. J., Boyer, M., Laurila, T., Brasseur, Z., Jozef, G., de Boer, G., Shupe, M. D., Henning, S., Bucci, S., Dütsch, M., Stohl, A., Petäjä, T., Daellenbach, K. R., Jokinen, T., and Schmale, J.: A central arctic extreme aerosol event triggered by a warm air-mass intrusion, *Nat. Commun.*, 13, <https://doi.org/10.1038/s41467-022-32872-2>, 2022.
- Dekoutsidis, G., Wirth, M., and Groß, S.: The effects of warm-air intrusions in the high Arctic on cirrus clouds, *Atmos. Chem. Phys.*, 24, 5971–5987, <https://doi.org/10.5194/acp-24-5971-2024>, 2024.
- Eleftheriadis, K., Vratolis, S., and Nyeki, S.: Aerosol black carbon in the European Arctic: Measurements at Zeppelin station, Ny-Ålesund, Svalbard from 1998–2007, *Geophys. Res. Lett.*, 36, <https://doi.org/10.1029/2008GL035741>, 2009.
- Engvall, A.-C., Krejci, R., Ström, J., Treffeisen, R., Scheele, R., Hermansen, O., and Paatero, J.: Changes in aerosol properties during spring-summer period in the Arctic troposphere, *Atmos. Chem. Phys.*, 8, 445–462, <https://doi.org/10.5194/acp-8-445-2008>, 2008.
- Fierce, L., Riemer, N., and Bond, T. C.: Explaining variance in black carbon’s aging timescale, *Atmos. Chem. Phys.*, 15, 3173–3191, <https://doi.org/10.5194/acp-15-3173-2015>, 2015.
- Fierce, L., Bond, T. C., Bauer, S. E., Mena, F., and Riemer, N.: Black carbon absorption at the global scale is affected by particle-scale diversity in composition, *Nat. Commun.*, 7, <https://doi.org/10.1038/ncomms12361>, 2016.
- Fierce, L., Onasch, T. B., Cappa, C. D., Mazzoleni, C., China, S., Bhandari, J., Davidovits, P., Al Fischer, D., Helgestad, T., Lambe, A. T., Sedlacek, A. J., Smith, G. D., and Wolff, L.: Radiative absorption enhancements by black carbon controlled by particle-to-particle heterogeneity in composition, *P. Natl. Acad. Sci. USA*, 117, 5196–5203, <https://doi.org/10.1073/pnas.1919723117>, 2020.
- Flanner, M. G.: Arctic climate sensitivity to local black carbon, *J. Geophys. Res.-Atmos.*, 118, 1840–1851, <https://doi.org/10.1002/jgrd.50176>, 2013.
- Flowers, B. A., Dubey, M. K., Mazzoleni, C., Stone, E. A., Schauer, J. J., Kim, S.-W., and Yoon, S. C.: Optical-chemical-microphysical relationships and closure studies for mixed carbonaceous aerosols observed at Jeju Island; 3-laser photoacoustic spectrometer, particle sizing, and filter analysis, *Atmos. Chem. Phys.*, 10, 10387–10398, <https://doi.org/10.5194/acp-10-10387-2010>, 2010.
- Fossum, K. N., Ovadnevaite, J., Liu, D., Flynn, M., O’Dowd, C., and Ceburnis, D.: Background levels of black carbon over remote marine locations, *Atmos. Res.*, 271, <https://doi.org/10.1016/j.atmosres.2022.106119>, 2022.
- Gao, R. S., Schwarz, J. P., Kelly, K. K., Fahey, D. W., Watts, L. A., Thompson, T. L., Spackman, J. R., Slowik, J. G., Cross, E. S., Han, J. H., Davidovits, P., Onasch, T. B., and Worsnop, D. R.: A novel method for estimating light-scattering properties of soot aerosols using a modified single-particle soot photometer, *Aerosol Sci. Technol.*, 41, 125–135, <https://doi.org/10.1080/02786820601118398>, 2007.
- Garrett, T. J., Brattström, S., Sharma, S., Worthy, D. E. J., and Novelli, P.: The role of scavenging in the seasonal transport of black carbon and sulfate to the Arctic, *Geophys. Res. Lett.*, 38, <https://doi.org/10.1029/2011GL048221>, 2011.
- Gogoi, M. M., Pandey, S. K., Arun, B. S., Nair, V. S., Thakur, R. C., Chaubey, J. P., Tiwari, A., Manoj, M. R., Kompalli, S. K., Vaishya, A., Prijith, S. S., Hegde, P., and Babu, S. S.: Long-term changes in aerosol radiative properties over Ny-Ålesund: Results from Indian scientific expeditions to the Arctic, *Polar Sci.*, 30, <https://doi.org/10.1016/j.polar.2021.100700>, 2021.
- Graham, R. M., Cohen, L., Petty, A. A., Boisvert, L. N., Rinke, A., Hudson, S. R., Nicolaus, M., and Granskog, M. A.: Increasing frequency and duration of Arctic winter warming events, *Geophys. Res. Lett.*, 44, 6974–6983, <https://doi.org/10.1002/2017GL073395>, 2017.
- Gustafsson, Ö., Budhavant, K., Chimurkar, N., Clarke, S., Dreyfus, G., Gong, X., Klimont, Z., Klingmüller, K., Kim, S. W., Lelieveld, J., Myhre, G., Nair, H. R. C. R., Peng, J., Ramanathan, V., Rana, A., Manoj, M. R., Satheesh, S. K., Venkataraman, C., and Zhang, Q.: Atmospheric black carbon in the climate system, *Nat. Rev. Earth Environ.*, <https://doi.org/10.1038/s43017-026-00773-3>, 2026.
- Gyawali, M., Arnott, W. P., Zaveri, R. A., Song, C., Flowers, B., Dubey, M. K., Setyan, A., Zhang, Q., China, S., Mazzoleni, C., Gorkowski, K., Subramanian, R., and Moosmüller, H.: Evolution of multispectral aerosol absorption properties in a biogenically-influenced urban environment during the CARES campaign, *Atmosphere*, 8, <https://doi.org/10.3390/atmos8110217>, 2017.
- Haywood, J. and Boucher, O.: Estimates of the direct and indirect radiative forcing due to tropospheric aerosols: a review, *Rev. Geophys.*, 38, 513–543, <https://doi.org/10.1029/1999RG000078>, 2000.
- Henderson, G. R., Barrett, B. S., Wachowicz, L. J., Mattingly, K. S., Preece, J. R., and Mote, T. L.: Local and Remote Atmospheric

- Circulation Drivers of Arctic Change: A Review, *Front. Earth Sci.* <https://doi.org/10.3389/feart.2021.709896>, 2021.
- Heutte, B., Bergner, N., Beck, I., Angot, H., Dada, L., Qu  l  ver, L. L. J., Laurila, T., Boyer, M., Brasseur, Z., Daellenbach, K. R., Henning, S., Kuang, C., Kulmala, M., Lampilahti, J., Lampim  ki, M., Pet  j  , T., Shupe, M. D., Sipil  , M., Uin, J., Jokinen, T., and Schmale, J.: Measurements of aerosol microphysical and chemical properties in the central Arctic atmosphere during MOSAiC, *Sci. Data*, 10, <https://doi.org/10.1038/s41597-023-02586-1>, 2023.
- Jur  nyi, Z., Zanutta, M., Lund, M., Samset, B., Skeie, R., Sharma, S., and Herber, A.: A climatology of Black Carbon properties in the Arctic, from a decade of spring and summertime aircraft measurements, *Research Square* [preprint], <https://doi.org/10.21203/rs.3.rs-1938170/v1>, 11 August 2022.
- Jur  nyi, Z., Zanutta, M., Lund, M. T., Samset, B. H., Skeie, R. B., Sharma, S., Wendisch, M., and Herber, A.: Atmospheric concentrations of black carbon are substantially higher in spring than summer in the Arctic, *Commun. Earth Environ.*, 4, <https://doi.org/10.1038/s43247-023-00749-x>, 2023.
- Kanzow, T.: Berichte zur Polar- und Meeresforschung, Bericht Nr. 770/2023, https://doi.org/10.57738/BzPM_0770_2023, 2023.
- Khalizov, A. F., Xue, H., Wang, L., Zheng, J., and Zhang, R.: Enhanced light absorption and scattering by carbon soot aerosol internally mixed with sulfuric acid, *J. Phys. Chem. A*, 113, 1066–1074, <https://doi.org/10.1021/jp807531n>, 2009.
- Ko, J., Krasowsky, T., and Ban-Weiss, G.: Measurements to determine the mixing state of black carbon emitted from the 2017–2018 California wildfires and urban Los Angeles, *Atmos. Chem. Phys.*, 20, 15635–15664, <https://doi.org/10.5194/acp-20-15635-2020>, 2020.
- Kompalli, S. K., Suresh Babu, S. N., Satheesh, S. K., Krishna Moorthy, K., Das, T., Boopathy, R., Liu, D., Darbyshire, E., Allan, J. D., Brooks, J., Flynn, M. J., and Coe, H.: Seasonal contrast in size distributions and mixing state of black carbon and its association with PM_{1.0} chemical composition from the eastern coast of India, *Atmos. Chem. Phys.*, 20, 3965–3985, <https://doi.org/10.5194/acp-20-3965-2020>, 2020.
- Kompalli, S. K., Babu, S. N. S., Moorthy, K. K., Satheesh, S. K., Gogoi, M. M., Nair, V. S., Jayachandran, V. N., Liu, D., Flynn, M. J., and Coe, H.: Mixing state of refractory black carbon aerosol in the South Asian outflow over the northern Indian Ocean during winter, *Atmos. Chem. Phys.*, 21, 9173–9199, <https://doi.org/10.5194/acp-21-9173-2021>, 2021.
- Kondo, Y., Sahu, L., Kuwata, M., Miyazaki, Y., Takegawa, N., Moteki, N., Imaru, J., Han, S., Nakayama, T., Oanh, N. T. K., Hu, M., Kim, Y. J., and Kita, K.: Stabilization of the mass absorption cross section of black carbon for filter-based absorption photometry by the use of a heated inlet, *Aerosol Sci. Technol.*, 43, 741–756, <https://doi.org/10.1080/02786820902889879>, 2009.
- Laborde, M., Schnaiter, M., Linke, C., Saathoff, H., Naumann, K.-H., M  hler, O., Berlenz, S., Wagner, U., Taylor, J. W., Liu, D., Flynn, M., Allan, J. D., Coe, H., Heimerl, K., Dahlk  tter, F., Weinzierl, B., Wollny, A. G., Zanutta, M., Cozic, J., Laj, P., Hiltnerberger, R., Schwarz, J. P., and Gysel, M.: Single Particle Soot Photometer intercomparison at the AIDA chamber, *Atmos. Meas. Tech.*, 5, 3077–3097, <https://doi.org/10.5194/amt-5-3077-2012>, 2012.
- Laborde, M., Crippa, M., Tritscher, T., Jur  nyi, Z., Decarlo, P. F., Temime-Roussel, B., Marchand, N., Eckhardt, S., Stohl, A., Baltensperger, U., Pr  v  t, A. S. H., Weingartner, E., and Gysel, M.: Black carbon physical properties and mixing state in the European megacity Paris, *Atmos. Chem. Phys.*, 13, 5831–5856, <https://doi.org/10.5194/acp-13-5831-2013>, 2013.
- Lack, D. A., Langridge, J. M., Bahreini, R., Cappa, C. D., Middlebrook, A. M., and Schwarz, J. P.: Brown carbon and internal mixing in biomass burning particles, *P. Natl. Acad. Sci. USA*, 109, 14802–14807, <https://doi.org/10.1073/pnas.1206575109>, 2012.
- Lan, Z. J., Huang, X. F., Yu, K. Y., Sun, T. Le, Zeng, L. W., and Hu, M.: Light absorption of black carbon aerosol and its enhancement by mixing state in an urban atmosphere in South China, *Atmos. Environ.*, 69, 118–123, <https://doi.org/10.1016/j.atmosenv.2012.12.009>, 2013.
- Lim, S., Lee, M., and Yoo, H. J.: Size distributions, mixing state, and morphology of refractory black carbon in an urban atmosphere of northeast Asia during summer, *Sci. Total Environ.*, 856, <https://doi.org/10.1016/j.scitotenv.2022.158436>, 2023.
- Linke, C., Ibrahim, I., Schleicher, N., Hiltnerberger, R., Andreae, M. O., Leisner, T., and Schnaiter, M.: A novel single-cavity three-wavelength photoacoustic spectrometer for atmospheric aerosol research, *Atmos. Meas. Tech.*, 9, 5331–5346, <https://doi.org/10.5194/amt-9-5331-2016>, 2016.
- Liu, D., Flynn, M., Gysel, M., Targino, A., Crawford, I., Bower, K., Choulaton, T., Jur  nyi, Z., Steinbacher, M., H  glin, C., Curtius, J., Kampus, M., Petzold, A., Weingartner, E., Baltensperger, U., and Coe, H.: Single particle characterization of black carbon aerosols at a tropospheric alpine site in Switzerland, *Atmos. Chem. Phys.*, 10, 7389–7407, <https://doi.org/10.5194/acp-10-7389-2010>, 2010.
- Liu, D., Allan, J. D., Young, D. E., Coe, H., Beddows, D., Fleming, Z. L., Flynn, M. J., Gallagher, M. W., Harrison, R. M., Lee, J., Prevot, A. S. H., Taylor, J. W., Yin, J., Williams, P. I., and Zotter, P.: Size distribution, mixing state and source apportionment of black carbon aerosol in London during wintertime, *Atmos. Chem. Phys.*, 14, 10061–10084, <https://doi.org/10.5194/acp-14-10061-2014>, 2014.
- Liu, D., Quennehen, B., Darbyshire, E., Allan, J. D., Williams, P. I., Taylor, J. W., Bauguitte, S. J.-B., Flynn, M. J., Lowe, D., Gallagher, M. W., Bower, K. N., Choulaton, T. W., and Coe, H.: The importance of Asia as a source of black carbon to the European Arctic during springtime 2013, *Atmos. Chem. Phys.*, 15, 11537–11555, <https://doi.org/10.5194/acp-15-11537-2015>, 2015.
- Liu, D., Joshi, R., Wang, J., Yu, C., Allan, J. D., Coe, H., Flynn, M. J., Xie, C., Lee, J., Squires, F., Kotthaus, S., Grimmond, S., Ge, X., Sun, Y., and Fu, P.: Contrasting physical properties of black carbon in urban Beijing between winter and summer, *Atmos. Chem. Phys.*, 19, 6749–6769, <https://doi.org/10.5194/acp-19-6749-2019>, 2019.
- Liu, H., Pan, X., Liu, D., Liu, X., Chen, X., Tian, Y., Sun, Y., Fu, P., and Wang, Z.: Mixing characteristics of refractory black carbon aerosols at an urban site in Beijing, *Atmos. Chem. Phys.*, 20, 5771–5785, <https://doi.org/10.5194/acp-20-5771-2020>, 2020.
- Liu, J., Fan, S., Horowitz, L. W., and Levy, H.: Evaluation of factors controlling long-range transport of black carbon to the Arctic, *J. Geophys. Res.-Atmos.*, 116, <https://doi.org/10.1029/2010JD015145>, 2011.

- Ludwig, V., Spreen, G., and Pedersen, L. T.: Evaluation of a new merged sea-ice concentration dataset at 1 km resolution from thermal infrared and passive microwave satellite data in the arctic, *Remote Sens.*, 12, 1–28, <https://doi.org/10.3390/rs12193183>, 2020.
- Ma, Y., Huang, C., Jabbour, H., Zheng, Z., Wang, Y., Jiang, Y., Zhu, W., Ge, X., Collier, S., and Zheng, J.: Mixing state and light absorption enhancement of black carbon aerosols in summertime Nanjing, China, *Atmos. Environ.*, 222, <https://doi.org/10.1016/j.atmosenv.2019.117141>, 2020.
- Matsui, H.: Black carbon simulations using a size- and mixing-state-resolved three-dimensional model: 1. Radiative effects and their uncertainties, *J. Geophys. Res.*, 121, 1793–1807, <https://doi.org/10.1002/2015JD023998>, 2016.
- McMeeking, G. R., Hamburger, T., Liu, D., Flynn, M., Morgan, W. T., Northway, M., Highwood, E. J., Krejci, R., Allan, J. D., Minikin, A., and Coe, H.: Black carbon measurements in the boundary layer over western and northern Europe, *Atmos. Chem. Phys.*, 10, 9393–9414, <https://doi.org/10.5194/acp-10-9393-2010>, 2010.
- Mortin, J., Svensson, G., Graversen, R. G., Kapsch, M. L., Stroeve, J. C., and Boisvert, L. N.: Melt onset over Arctic sea ice controlled by atmospheric moisture transport, *Geophys. Res. Lett.*, 43, 6636–6642, <https://doi.org/10.1002/2016GL069330>, 2016.
- Moteki, N. and Kondo, Y.: Dependence of laser-induced incandescence on physical properties of black carbon aerosols: Measurements and theoretical interpretation, *Aerosol Sci. Tech.*, 44, 663–675, <https://doi.org/10.1080/02786826.2010.484450>, 2010.
- Moteki, N., Kondo, Y., and Nakamura, S.-I.: Method to measure refractive indices of small nonspherical particles: Application to black carbon particles, *J. Aerosol. Sci.*, 41, 513–521, <https://doi.org/10.1016/j.jaerosci.2010.02.013>, 2010.
- Moteki, N., Kondo, Y., Oshima, N., Takegawa, N., Koike, M., Kita, K., Matsui, H., and Kajino, M.: Size dependence of wet removal of black carbon aerosols during transport from the boundary layer to the free troposphere, *Geophys. Res. Lett.*, 39, <https://doi.org/10.1029/2012GL052034>, 2012.
- Moteki, N., Ohata, S., Yoshida, A., and Adachi, K.: Constraining the complex refractive index of black carbon particles using the complex forward-scattering amplitude, *Aerosol Sci. Tech.*, 57, 678–699, <https://doi.org/10.1080/02786826.2023.2202243>, 2023.
- Motos, G., Schmale, J., Corbin, J. C., Zanatta, M., Baltensperger, U., and Gysel-Beer, M.: Droplet activation behaviour of atmospheric black carbon particles in fog as a function of their size and mixing state, *Atmos. Chem. Phys.*, 19, 2183–2207, <https://doi.org/10.5194/acp-19-2183-2019>, 2019a.
- Motos, G., Schmale, J., Corbin, J. C., Modini, R. L., Karlen, N., Bertò, M., Baltensperger, U., and Gysel-Beer, M.: Cloud droplet activation properties and scavenged fraction of black carbon in liquid-phase clouds at the high-alpine research station Jungfraujoch (3580 m a.s.l.), *Atmos. Chem. Phys.*, 19, 3833–3855, <https://doi.org/10.5194/acp-19-3833-2019>, 2019b.
- Motos, G., Corbin, J. C., Schmale, J., Modini, R. L., Bertò, M., Kupiszewski, P., Baltensperger, U., and Gysel-Beer, M.: Black Carbon Aerosols in the Lower Free Troposphere are Heavily Coated in Summer but Largely Uncoated in Winter at Jungfraujoch in the Swiss Alps, *Geophys. Res. Lett.*, 47, <https://doi.org/10.1029/2020GL088011>, 2020.
- Müller, K., Lehmann, S., van Pinxteren, D., Gnauk, T., Niedermeier, N., Wiedensohler, A., and Herrmann, H.: Particle characterization at the Cape Verde atmospheric observatory during the 2007 RHaMBLe intensive, *Atmos. Chem. Phys.*, 10, 2709–2721, <https://doi.org/10.5194/acp-10-2709-2010>, 2010.
- Müller, T., Laborde, M., Kassell, G., and Wiedensohler, A.: Design and performance of a three-wavelength LED-based total scatter and backscatter integrating nephelometer, *Atmos. Meas. Tech.*, 4, 1291–1303, <https://doi.org/10.5194/amt-4-1291-2011>, 2011.
- Nenes, A., Conant, W. C., and Seinfeld, J. H.: Black carbon radiative heating effects on cloud microphysics and implications for the aerosol indirect effect 2. Cloud microphysics, *J. Geophys. Res.-Atmos.*, 107, <https://doi.org/10.1029/2002jd002101>, 2002.
- Nithin, B., Kompalli, S. K., and Babu, S. S.: Black carbon mixing state and light-absorption enhancement under different air mass regimes over a tropical coastal site, *Atmos. Res.*, 331, <https://doi.org/10.1016/j.atmosres.2025.108641>, 2026.
- Pan, X., Zhang, Y., Xue, C., Kuhn, U., Hrabec de Angelis, I., Pöhler, C., Ditas, J., Heins, L., Aardema, H. M., Slagter, H. A., Calleja, M. L., Dragoneas, A., Walter, D., Nillius, B., Wang, Q., Ma, N., Su, H., Pöschl, U., Haug, G. H., Schiebel, R., and Cheng, Y.: Black Carbon in the Marine Atmosphere: Concentration and Mixing State From Coastal to Remote Atlantic Regions, *J. Geophys. Res.-Atmos.*, 131, <https://doi.org/10.1029/2025JD045346>, 2026.
- Pandolfi, M., Alados-Arboledas, L., Alastuey, A., Andrade, M., Angelov, C., Artiñano, B., Backman, J., Baltensperger, U., Bonasoni, P., Bukowiecki, N., Collaud Coen, M., Conil, S., Coz, E., Crenn, V., Dudoitis, V., Ealo, M., Eleftheriadis, K., Favez, O., Fetfatzis, P., Fiebig, M., Flentje, H., Ginot, P., Gysel, M., Henzing, B., Hoffer, A., Holubova Smejkalova, A., Kalapov, I., Kalivitis, N., Kouvarakis, G., Kristensson, A., Kulmala, M., Lihavainen, H., Lunder, C., Luoma, K., Lyamani, H., Marinoni, A., Mihalopoulos, N., Moerman, M., Nicolas, J., O’Dowd, C., Petäjä, T., Petit, J.-E., Pichon, J. M., Prokopciuk, N., Putaud, J.-P., Rodríguez, S., Sciare, J., Sellegri, K., Swietlicki, E., Titos, G., Tuch, T., Tunved, P., Ulevicius, V., Vaishya, A., Vana, M., Virkkula, A., Vratolis, S., Weingartner, E., Wiedensohler, A., and Laj, P.: A European aerosol phenomenology – 6: scattering properties of atmospheric aerosol particles from 28 ACTRIS sites, *Atmos. Chem. Phys.*, 18, 7877–7911, <https://doi.org/10.5194/acp-18-7877-2018>, 2018.
- Park, J., Dall’Osto, M., Park, K., Gim, Y., Kang, H. J., Jang, E., Park, K.-T., Park, M., Yum, S. S., Jung, J., Lee, B. Y., and Yoon, Y. J.: Shipborne observations reveal contrasting Arctic marine, Arctic terrestrial and Pacific marine aerosol properties, *Atmos. Chem. Phys.*, 20, 5573–5590, <https://doi.org/10.5194/acp-20-5573-2020>, 2020.
- Pernov, J. B., Beddows, D., Thomas, D. C., Dall’Osto, M., Harrison, R. M., Schmale, J., Skov, H., and Massling, A.: Increased aerosol concentrations in the High Arctic attributable to changing atmospheric transport patterns, *NPJ Clim. Atmos. Sci.*, 5, <https://doi.org/10.1038/s41612-022-00286-y>, 2022.
- Petzold, A. and Schönlinner, M.: Multi-angle absorption photometry – A new method for the measurement of aerosol light absorption and atmospheric black carbon, *J. Aerosol Sci.*, 35, 421–441, <https://doi.org/10.1016/j.jaerosci.2003.09.005>, 2004.
- Popovicheva, O. B., Evangelidou, N., Eleftheriadis, K., Kalogridis, A. C., Sitnikov, N., Eckhardt, S., and Stohl, A.:

- Black Carbon Sources Constrained by Observations in the Russian High Arctic, *Environ. Sci. Technol.*, 51, 3871–3879, <https://doi.org/10.1021/acs.est.6b05832>, 2017.
- Quinn, P. K., Miller, T. L., Bates, T. S., Ogren, J. A., Andrews, E., and Shaw, G. E.: A 3-year record of simultaneously measured aerosol chemical and optical properties at Barrow, Alaska, *J. Geophys. Res.-Atmos.*, 107, <https://doi.org/10.1029/2001jd001248>, 2002.
- Quinn, P. K., Bates, T. S., Baum, E., Doubleday, N., Fiore, A. M., Flanner, M., Fridlind, A., Garrett, T. J., Koch, D., Menon, S., Shindell, D., Stohl, A., and Warren, S. G.: Short-lived pollutants in the Arctic: their climate impact and possible mitigation strategies, *Atmos. Chem. Phys.*, 8, 1723–1735, <https://doi.org/10.5194/acp-8-1723-2008>, 2008.
- Raatikainen, T., Brus, D., Hyvärinen, A.-P., Svensson, J., Asmi, E., and Lihavainen, H.: Black carbon concentrations and mixing state in the Finnish Arctic, *Atmos. Chem. Phys.*, 15, 10057–10070, <https://doi.org/10.5194/acp-15-10057-2015>, 2015.
- Raatikainen, T., Brus, D., Hooda, R. K., Hyvärinen, A.-P., Asmi, E., Sharma, V. P., Arola, A., and Lihavainen, H.: Size-selected black carbon mass distributions and mixing state in polluted and clean environments of northern India, *Atmos. Chem. Phys.*, 17, 371–383, <https://doi.org/10.5194/acp-17-371-2017>, 2017.
- Rantanen, M., Karpechko, A. Y., Lipponen, A., Nordling, K., Hyvärinen, O., Ruosteenoja, K., Vihma, T., and Laaksonen, A.: The Arctic has warmed nearly four times faster than the globe since 1979, *Commun. Earth Environ.*, 3, <https://doi.org/10.1038/s43247-022-00498-3>, 2022.
- Romshoo, B., Patil, J., Michels, T., Müller, T., Kloft, M., and Pöhlker, M.: Improving the predictions of black carbon (BC) optical properties at various aging stages using a machine-learning-based approach, *Atmos. Chem. Phys.*, 24, 8821–8846, <https://doi.org/10.5194/acp-24-8821-2024>, 2024.
- Rose, T., Crewell, S., Löhner, U., and Simmer, C.: A network suitable microwave radiometer for operational monitoring of the cloudy atmosphere, *Atmos. Res.*, 75, 183–200, <https://doi.org/10.1016/j.atmosres.2004.12.005>, 2005.
- Sand, M., Berntsen, T. K., Seland, Ø., and Kristjánsson, J. E.: Arctic surface temperature change to emissions of black carbon within Arctic or midlatitudes, *J. Geophys. Res.-Atmos.*, 118, 7788–7798, <https://doi.org/10.1002/jgrd.50613>, 2013.
- Schmale, J., Arnold, S. R., Law, K. S., Thorp, T., Anenberg, S., Simpson, W. R., Mao, J., and Pratt, K. A.: Local Arctic Air Pollution: A Neglected but Serious Problem, *Earths Future*, 6, 1385–1412, <https://doi.org/10.1029/2018EF000952>, 2018.
- Schmale, J., Zieger, P., and Ekman, A. M. L.: Aerosols in current and future Arctic climate, *Nat. Clim. Chang.*, 11, 95–105, <https://doi.org/10.1038/s41558-020-00969-5>, 2021.
- Schmale, J., Sharma, S., Decesari, S., Pernov, J., Massling, A., Hansson, H.-C., von Salzen, K., Skov, H., Andrews, E., Quinn, P. K., Upchurch, L. M., Eleftheriadis, K., Traversi, R., Gilarioni, S., Mazzola, M., Laing, J., and Hopke, P.: Pan-Arctic seasonal cycles and long-term trends of aerosol properties from 10 observatories, *Atmos. Chem. Phys.*, 22, 3067–3096, <https://doi.org/10.5194/acp-22-3067-2022>, 2022.
- Schmeisser, L., Backman, J., Ogren, J. A., Andrews, E., Asmi, E., Starkweather, S., Uttal, T., Fiebig, M., Sharma, S., Eleftheriadis, K., Vratolis, S., Bergin, M., Tunved, P., and Jefferson, A.: Seasonality of aerosol optical properties in the Arctic, *Atmos. Chem. Phys.*, 18, 11599–11622, <https://doi.org/10.5194/acp-18-11599-2018>, 2018.
- Schnaiter, M., Linke, C., Möhler, O., Naumann, K. H., Saathoff, H., Wagner, R., Schurath, U., and Wehner, B.: Absorption amplification of black carbon internally mixed with secondary organic aerosol, *J. Geophys. Res.-Atmos.*, 110, 1–11, <https://doi.org/10.1029/2005JD006046>, 2005.
- Schulz, H., Zanatta, M., Bozem, H., Leaitch, W. R., Herber, A. B., Burkart, J., Willis, M. D., Kunkel, D., Hoor, P. M., Abbatt, J. P. D., and Gerdes, R.: High Arctic aircraft measurements characterising black carbon vertical variability in spring and summer, *Atmos. Chem. Phys.*, 19, 2361–2384, <https://doi.org/10.5194/acp-19-2361-2019>, 2019.
- Schwarz, J. P., Gao, R. S., Spackman, J. R., Watts, L. A., Thomson, D. S., Fahey, D. W., Ryerson, T. B., Peischl, J., Holloway, J. S., Trainer, M., Frost, G. J., Baynard, T., Lack, D. A., de Gouw, J. A., Warneke, C., and Del Negro, L. A.: Measurement of the mixing state, mass, and optical size of individual black carbon particles in urban and biomass burning emissions, *Geophys. Res. Lett.*, 35, <https://doi.org/10.1029/2008GL033968>, 2008.
- Seinfeld, J. H. and Pandis, S. N.: *Atmospheric Chemistry and Physics – From Air Pollution to Climate Change*, 2nd Edn., John Wiley & Sons, New Jersey, ISBN 13 978-0-471-72018-8, 2006.
- Sharma, S., Andrews, E., Barrie, L. A., Ogren, J. A., and Lavoué, D.: Variations and sources of the equivalent black carbon in the high Arctic revealed by long-term observations at Alert and Barrow: 1989–2003, *J. Geophys. Res.-Atmos.*, 111, <https://doi.org/10.1029/2005JD006581>, 2006.
- Sharma, S., Leaitch, W. R., Huang, L., Veber, D., Kolonjari, F., Zhang, W., Hanna, S. J., Bertram, A. K., and Ogren, J. A.: An evaluation of three methods for measuring black carbon in Alert, Canada, *Atmos. Chem. Phys.*, 17, 15225–15243, <https://doi.org/10.5194/acp-17-15225-2017>, 2017.
- Shiraiwa, M., Kondo, Y., Moteki, N., Takegawa, N., Miyazaki, Y., and Blake, D. R.: Evolution of mixing state of black carbon in polluted air from Tokyo, *Geophys. Res. Lett.*, 34, <https://doi.org/10.1029/2007GL029819>, 2007.
- Shiraiwa, M., Kondo, Y., Moteki, N., Takegawa, N., Sahu, L. K., Takami, A., Hatakeyama, S., Yonemura, S., and Blake, D. R.: Radiative impact of mixing state of black carbon aerosol in Asian outflow, *J. Geophys. Res.-Atmos.*, 113, <https://doi.org/10.1029/2008JD010546>, 2008.
- Shiraiwa, M., Kondo, Y., Iwamoto, T., and Kita, K.: Amplification of light absorption of black carbon by organic coating, *Aerosol Sci. Technol.*, 44, 46–54, <https://doi.org/10.1080/02786820903357686>, 2010.
- Spreen, G., Kaleschke, L., and Heygster, G.: Sea ice remote sensing using AMSR-E 89-GHz channels, *J. Geophys. Res.-Oceans*, 113, <https://doi.org/10.1029/2005JC003384>, 2008.
- Stein, A. F., Draxler, R. R., Rolph, G. D., Stunder, B. J. B., Cohen, M. D., and Ngan, F.: NOAA's hysplit atmospheric transport and dispersion modeling system, *B. Am. Meteorol. Soc.*, <https://doi.org/10.1175/BAMS-D-14-00110.1>, 2015.
- Stohl, A.: Characteristics of atmospheric transport into the Arctic troposphere, *J. Geophys. Res.-Atmos.*, 111, <https://doi.org/10.1029/2005JD006888>, 2006.
- Stohl, A., Klimont, Z., Eckhardt, S., Kupiainen, K., Shevchenko, V. P., Kopeikin, V. M., and Novigatsky, A. N.: Black carbon in the Arctic: the underestimated role of gas flaring and residen-

- tial combustion emissions, *Atmos. Chem. Phys.*, 13, 8833–8855, <https://doi.org/10.5194/acp-13-8833-2013>, 2013.
- Taketani, F., Miyakawa, T., Takashima, H., Komazaki, Y., Pan, X., Kanaya, Y., and Inoue, J.: Shipborne observations of atmospheric black carbon aerosol particles over the Arctic Ocean, Bering Sea, and North Pacific Ocean during september 2014, *J. Geophys. Res.*, 121, 1914–1921, <https://doi.org/10.1002/2015JD023648>, 2016.
- Taylor, J. W., Allan, J. D., Allen, G., Coe, H., Williams, P. I., Flynn, M. J., Le Breton, M., Muller, J. B. A., Percival, C. J., Oram, D., Forster, G., Lee, J. D., Rickard, A. R., Parrington, M., and Palmer, P. I.: Size-dependent wet removal of black carbon in Canadian biomass burning plumes, *Atmos. Chem. Phys.*, 14, 13755–13771, <https://doi.org/10.5194/acp-14-13755-2014>, 2014.
- Thackeray, C. W. and Hall, A.: An emergent constraint on future Arctic sea-ice albedo feedback, *Nat. Clim. Change*, 9, 972–978, <https://doi.org/10.1038/s41558-019-0619-1>, 2019.
- Thakur, R. C., Arun, B. S., Gogoi, M. M., Thamban, M., Thayyen, R. J., Redkar, B. L., and Suresh Babu, S.: Multi-layer distribution of Black Carbon and inorganic ions in the snowpacks of western Himalayas and snow albedo forcing, *Atmos. Environ.*, 261, <https://doi.org/10.1016/j.atmosenv.2021.118564>, 2021.
- Tinorua, S., Denjean, C., Nabat, P., Bourrienne, T., Pont, V., Gheusi, F., and Leclerc, E.: Higher absorption enhancement of black carbon in summer shown by 2-year measurements at the high-altitude mountain site of Pic du Midi Observatory in the French Pyrenees, *Atmos. Chem. Phys.*, 24, 1801–1824, <https://doi.org/10.5194/acp-24-1801-2024>, 2024.
- Tomasi, C., Vitale, V., Lupi, A., Di Carmine, C., Campanelli, M., Herber, A., Treffeisen, R., Stone, R. S., Andrews, E., Sharma, S., Radionov, V., von Hoyningen-Huene, W., Stebel, K., Hansen, G. H., Myhre, C. L., Wehrli, C., Aaltonen, V., Lihavainen, H., Virkkula, A., Hillamo, R., Ström, J., Toledano, C., Cachorro, V. E., Ortiz, P., de Frutos, A. M., Blindheim, S., Frioud, M., Gausa, M., Zielinski, T., Petelski, T., and Yamanouchi, T.: Aerosols in polar regions: A historical overview based on optical depth and in situ observations, *J. Geophys. Res.-Atmos.* <https://doi.org/10.1029/2007JD008432>, 2007.
- Tunved, P., Ström, J., and Krejci, R.: Arctic aerosol life cycle: linking aerosol size distributions observed between 2000 and 2010 with air mass transport and precipitation at Zeppelin station, Ny-Ålesund, Svalbard, *Atmos. Chem. Phys.*, 13, 3643–3660, <https://doi.org/10.5194/acp-13-3643-2013>, 2013.
- Ueda, S., Nakayama, T., Taketani, F., Adachi, K., Matsuki, A., Iwamoto, Y., Sadanaga, Y., and Matsumi, Y.: Light absorption and morphological properties of soot-containing aerosols observed at an East Asian outflow site, Noto Peninsula, Japan, *Atmos. Chem. Phys.*, 16, 2525–2541, <https://doi.org/10.5194/acp-16-2525-2016>, 2016.
- Walbröl, A., Crewell, S., Engelmann, R., Orlandi, E., Griesche, H., Radenz, M., Hofer, J., Althausen, D., Maturilli, M., and Ebell, K.: Atmospheric temperature, water vapour and liquid water path from two microwave radiometers during MOSAiC, *Sci. Data*, 9, <https://doi.org/10.1038/s41597-022-01504-1>, 2022.
- Wang, Q., Cao, J., Han, Y., Tian, J., Zhu, C., Zhang, Y., Zhang, N., Shen, Z., Ni, H., Zhao, S., and Wu, J.: Sources and physicochemical characteristics of black carbon aerosol from the southeastern Tibetan Plateau: internal mixing enhances light absorption, *Atmos. Chem. Phys.*, 18, 4639–4656, <https://doi.org/10.5194/acp-18-4639-2018>, 2018.
- Wang, Q. Y., Huang, R.-J., Cao, J. J., Tie, X. X., Ni, H. Y., Zhou, Y. Q., Han, Y. M., Hu, T. F., Zhu, C. S., Feng, T., Li, N., and Li, J. D.: Black carbon aerosol in winter northeastern Qinghai–Tibetan Plateau, China: the source, mixing state and optical property, *Atmos. Chem. Phys.*, 15, 13059–13069, <https://doi.org/10.5194/acp-15-13059-2015>, 2015.
- Wang, Y., Li, W., Huang, J., Liu, L., Pang, Y., He, C., Liu, F., Liu, D., Bi, L., Zhang, X., and Shi, Z.: Nonlinear Enhancement of Radiative Absorption by Black Carbon in Response to Particle Mixing Structure, *Geophys. Res. Lett.*, 48, <https://doi.org/10.1029/2021GL096437>, 2021.
- Wendisch, M., Brückner, M., Crewell, S., Ehrlich, A., Notholt, J., Lüpkes, C., Macke, A., Burrows, J. P., Rinke, A., Quaas, J., Maturilli, M., Schemann, V., Shupe, M. D., Akansu, E. F., Barrientos-Velasco, C., Bärffuss, K., Blechschmidt, A.-M., Block, K., Bougoudis, I., Bozem, H., Böckmann, C., Bracher, A., Bresson, H., Bretschneider, L., Buschmann, M., Chechin, D. G., Chylik, J., Dahlke, S., Deneke, H., Dethloff, K., Donth, T., Dorn, W., Dupuy, R., Ebell, K., Egerer, U., Engelmann, R., Eppers, O., Gerdes, R., Gierens, R., Gorodetskaya, I. V., Gottschalk, M., Griesche, H., Gryanik, V. M., Handorf, D., Harm-Altstädter, B., Hartmann, J., Hartmann, M., Heinold, B., Herber, A., Herrmann, H., Heygster, G., Höschel, I., Hofmann, Z., Hölemann, J., Hünnerbein, A., Jafariserajehlou, S., Jäkel, E., Jacobi, C., Janout, M., Jansen, F., Jourdan, O., Jurányi, Z., Kalesse-Los, H., Kanzow, T., Käthner, R., Kliesch, L. L., Klingebiel, M., Knudsen, E. M., Kovács, T., Körtke, W., Krampe, D., Kretzschmar, J., Kreyling, D., Kulla, B., Kunkel, D., Lampert, A., Lauer, M., Lelli, L., von Lerber, A., Linke, O., Löhnert, U., Lonardi, M., Losa, S. N., Losch, M., Maahn, M., Mech, M., Mei, L., Mertes, S., Metzner, E., Mewes, D., Michaelis, J., Mioche, G., Moser, M., Nakoudi, K., Neggers, R., Neuber, R., Nomokonova, T., Oelker, J., Papakonstantinou-Presvelou, I., Pätzold, F., Pefanis, V., Pohl, C., van Pinxteren, M., Radovan, A., Rhein, M., Rex, M., Richter, A., Risse, N., Ritter, C., Rostovsky, P., Rozanov, V. V., Ruiz Donoso, E., Saavedra-Garfias, P., Salzmann, M., Schacht, J., Schäfer, M., Schneider, J., Schnierstein, N., Seifert, P., Seo, S., Siebert, H., Soppa, M. A., Spreen, G., Stachlewska, I. S., Stapf, J., Stratmann, F., Tegen, I., Viceto, C., Voigt, C., Vountas, M., Walbröl, A., Walter, M., Wehner, B., Wex, H., Willmes, S., Zanutta, M., and Zeppenfeld, S.: Atmospheric and Surface Processes, and Feedback Mechanisms Determining Arctic Amplification: A Review of First Results and Prospects of the (AC)³ Project, *B. Am. Meteorol. Soc.*, 104, E208–E242, <https://doi.org/10.1175/BAMS-D-21-0218.1>, 2023.
- Winiger, P., Andersson, A., Eckhardt, S., Stohl, A., Semiletov, I. P., Dudarev, O. V., Charkin, A., Shakhova, N., Klimont, Z., Heyes, C., and Gustafsson, Ö.: Siberian Arctic black carbon sources constrained by model and observation, *P. Natl. Acad. Sci. USA*, 114, E1054–E1061, <https://doi.org/10.1073/pnas.1613401114>, 2017.
- Woods, C. and Caballero, R.: The role of moist intrusions in winter arctic warming and sea ice decline, *J. Climate*, 29, 4473–4485, <https://doi.org/10.1175/JCLI-D-15-0773.1>, 2016.
- Wu, C., Wu, D., and Yu, J. Z.: Quantifying black carbon light absorption enhancement with a novel statistical approach, *Atmos. Chem. Phys.*, 18, 289–309, <https://doi.org/10.5194/acp-18-289-2018>, 2018.

- Yang, Y.: Assessing Absorption Enhancement in Black Carbon: Insights into Mixing State Heterogeneity, Zenodo [data set], Zenodo. <https://doi.org/10.5281/zenodo.17312995>, 2024.
- Yang, Y., Müller, T., Poulain, L., Atabakhsh, S., Holanda, B. A., Voigtländer, J., Arora, S., and Pöhlker, M. L.: Microphysical properties of refractory black carbon aerosols for different air masses at a central European background site, *Atmos. Chem. Phys.*, 25, 8637–8655, <https://doi.org/10.5194/acp-25-8637-2025>, 2025.
- Zanatta, M., Gysel, M., Bukowiecki, N., Müller, T., Weingartner, E., Areskoug, H., Fiebig, M., Yttri, K. E., Mihalopoulos, N., Kouvarakis, G., Beddows, D., Harrison, R. M., Cavalli, F., Putaud, J. P., Spindler, G., Wiedensohler, A., Alastuey, A., Pandolfi, M., Sellegri, K., Swietlicki, E., Jaffrezo, J. L., Baltensperger, U., and Laj, P.: A European aerosol phenomenology-5: Climatology of black carbon optical properties at 9 regional background sites across Europe, *Atmos. Environ.*, 145, 346–364, <https://doi.org/10.1016/j.atmosenv.2016.09.035>, 2016.
- Zanatta, M., Laj, P., Gysel, M., Baltensperger, U., Vratolis, S., Eleftheriadis, K., Kondo, Y., Dubuisson, P., Winiarek, V., Kazadzis, S., Tunved, P., and Jacobi, H.-W.: Effects of mixing state on optical and radiative properties of black carbon in the European Arctic, *Atmos. Chem. Phys.*, 18, 14037–14057, <https://doi.org/10.5194/acp-18-14037-2018>, 2018.
- Zanatta, M., Mertes, S., Jourdan, O., Dupuy, R., Järvinen, E., Schnaiter, M., Eppers, O., Schneider, J., Jurányi, Z., and Herber, A.: Airborne investigation of black carbon interaction with low-level, persistent, mixed-phase clouds in the Arctic summer, *Atmos. Chem. Phys.*, 23, 7955–7973, <https://doi.org/10.5194/acp-23-7955-2023>, 2023.
- Zeng, L., Tan, T., Zhao, G., Du, Z., Hu, S., Shang, D., and Hu, M.: Overestimation of black carbon light absorption due to mixing state heterogeneity, *NPJ Clim. Atmos. Sci.*, 7, <https://doi.org/10.1038/s41612-023-00535-8>, 2024.
- Zhai, J., Yang, X., Li, L., Bai, B., Liu, P., Huang, Y., Fu, T. M., Zhu, L., Zeng, Z., Tao, S., Lu, X., Ye, X., Wang, X., Wang, L., and Chen, J.: Absorption Enhancement of Black Carbon Aerosols Constrained by Mixing-State Heterogeneity, *Environ. Sci. Technol.*, 56, 1586–1593, <https://doi.org/10.1021/acs.est.1c06180>, 2022.
- Zhang, Y., Cheng, X., Liu, J., and Hui, F.: The potential of sea ice leads as a predictor for summer Arctic sea ice extent, *The Cryosphere*, 12, 3747–3757, <https://doi.org/10.5194/tc-12-3747-2018>, 2018a.
- Zhang, Y., Favez, O., Canonaco, F., Liu, D., Močnik, G., Amodeo, T., Sciare, J., Prévôt, A. S. H., Gros, V., and Albinet, A.: Evidence of major secondary organic aerosol contribution to lensing effect black carbon absorption enhancement, *NPJ Clim. Atmos. Sci.*, 1, <https://doi.org/10.1038/s41612-018-0056-2>, 2018b.
- Zhang, Y., Su, H., Kecorius, S., Ma, N., Wang, Z., Sun, Y., Zhang, Q., Pöschl, U., Wiedensohler, A., Andreae, M. O., and Cheng, Y.: Extremely low-volatility organic coating leads to underestimation of black carbon climate impact, *One Earth*, 6, 158–166, <https://doi.org/10.1016/j.oneear.2023.01.009>, 2023.
- Zhang, Z., Wang, J., Riemer, N., Liu, C., Wang, J., Jin, Y., Tian, Z., Chen, G., Wang, B., Huang, X., Ding, A., and Wang, S.: Inversion Approach for Inferring Mixing State and Improving Optical Estimation of Coated Black Carbon Using Bulk-Volume Variables and Number-Size Distributions, *Environ. Sci. Technol.*, 60, 3998–4007, <https://doi.org/10.1021/acs.est.5c10094>, 2026.
- Zhao, C. and Garrett, T. J.: Effects of Arctic haze on surface cloud radiative forcing, *Geophys. Res. Lett.*, 42, 557–564, <https://doi.org/10.1002/2014GL062015>, 2015.
- Zieger, P., Heslin-Rees, D., Karlsson, L., Koike, M., Modini, R., and Krejci, R.: Black carbon scavenging by low-level Arctic clouds, *Nat. Commun.*, 14, <https://doi.org/10.1038/s41467-023-41221-w>, 2023.

Remarks from the typesetter

- TS1** Thank you very much for your feedback. Please note that not all changes could be inserted. The proofreading process is reserved for responses to the publisher remarks and, if applicable, spotting clear mistakes included during the production process. Updates to the manuscript content cannot be accepted and a further proofreading round is not foreseen (https://publications.copernicus.org/for_authors/proofreading_guidelines.html).
- TS2** Please give an explanation of why this needs to be changed. We have to ask the handling editor for approval. Thanks.
- TS3** Please give an explanation of why this needs to be changed. We have to ask the handling editor for approval. Thanks.
- TS4** Please give an explanation of why this needs to be changed. We have to ask the handling editor for approval. Thanks.
- TS5** Please add Zhai et al., 2021 to the reference list.
- TS6** Please also provide information what was changed in the Supplement as it may also need to be approved by the editor. Thanks.